MAGNETIC AND STRUCTURAL PROPERTIES OF NI-MN-GA FILMS

PRODUCED VIA PHYSICAL VAPOR TRI-DEPOSITION

by

Christopher Kimo Wilson

A thesis

submitted in partial fulfillment

of the requirements for the degree of

Master of Science in Materials Science & Engineering

Boise State University

August 2013

BOISE STATE UNIVERSITY GRADUATE COLLEGE

DEFENSE COMMITTEE AND FINAL READING APPROVALS

of the thesis submitted by

Christopher Kimo Wilson

Thesis Title: Magnetic and structural properties of Ni-Mn-Ga films produced via physical vapor tri-deposition

Date of Final Oral Examination: 17 June 2013

The following individuals read and discussed the thesis submitted by student Christopher Kimo Wilson, and they evaluated his presentation and response to questions during the final oral examination. They found that the student passed the final oral examination.

Peter Müllner, Ph.D.   Chair, Supervisory Committee

William B. Knowlton, Ph.D.   Member, Supervisory Committee

Dmitri Tenne, Ph.D.   Member, Supervisory Committee

The final reading approval of the thesis was granted by Peter Müllner, Ph.D., Chair of the Supervisory Committee. The thesis was approved for the Graduate College by John R. Pelton, Ph.D., Dean of the Graduate College.

ACKNOWLEDGEMENTS

ABSTRACT

The structural, thermal, magnetic, and mechanical properties of Ni-Mn-Ga magnetic shape-memory alloys depend strongly on composition. Compositions of sputter deposited films differ from the composition of the single alloy targets from which they originate, where the composition change depends on sputter parameters. Films produced via physical vapor deposition from single alloy targets have sound film-substrate adhesion and film uniformity, however, accurate control of composition is difficult. Tri-sputter deposition from multiple targets allows the flexibility of varying deposition rates and film compositions. A robust procedure with three targets (nickel, nickel-gallium, and manganese) was developed to deposit Ni-Mn-Ga films on silicon with defined composition, structural and magnetic properties. The sputter power was controlled and varied independently and systematically for each target. A film with a targeted composition of $Ni_{50}Mn_{28.6}Ga_{21.4}$ at. % Energy-Dispersive X-ray Spectroscopy (EDS) yielded the composition $Ni_{50.5}Mn_{29.2}Ga_{20.3}$ at.-%. X-Ray Diffraction (XRD) and Transmission Electron Microscopy (TEM) revealed the 14M modulated martensite structure, a <211> fiber texture, an average grain size of approximately 100 nm. The martensitic start and finish temperatures, measured with multi-beam optical sensor wafer curvature deflectometry, were 122 °C and 81 °C respectively, indicating stress-induced martensite formation at high temperature. Tri-deposition using three targets provides a method to control composition of Ni-Mn-Ga films and adjust film properties such as martensite structure and transformation temperature via target power adjustment.

TABLE OF CONTENTS

LIST OF TABLES

LIST OF FIGURES

LIST OF ABBREVIATIONS

SMA	Shape Memory Alloy
FSMA	Ferromagnetic Shape Memory Alloy
MFIS	Magnetic Field Induced Strain
PVD	Physical Vapor Deposition
DC	Direct Current
RF	Radio Frequency
MSMA	Magnetic Shape Memory Alloy
DOE	Design of Experiment
EDS	Energy-Dispersive X-Ray Spectroscope
SEM	Scanning Electron Microscope
VSM	Vibrating Sample Magnetometer
MOS	Multi-Beam Optical Sensor
CCD	Closed Circuit Detector
XRD	X-Ray Diffraction
FIB	Focused Ion Beam
LMIS	Liquid Metal Ion Source

EBSD   Electron Backscatter Diffraction

TEM   Transmission Electron Microscope

CHAPTER 1: INTRODUCTION

In the past fifty years, materials science has shifted focus from strength and mechanical properties of materials to functional materials for use as devices. Material properties such as magnetic, thermal, and electrical can be used in a material for contactless actuation control of large deformations not easily achievable by other actuators. In 1903, Friedrich Heusler, a German mining engineer and chemist, discovered a special group of intermetallics now known as Heusler phases, which are ferromagnetic though the constituting elements are not [1]. Sixty years later in a Naval Ordnance Lab, 12 intermetallic alloys, including Nickel Titanium (NiTi), were being investigated. Testing of NiTi revealed temperature dependent, significant length changes after annealing [2]. A shape memory alloy (SMA), like NiTi, is a class of functional materials that "remembers" its original shape and can change their shape under the application of an external field such as thermal, electrical, or magnetic. Thermally active SMAs like NiTi, exhibit plastic deformation up to 10%, which is recovered by heating through the martensite to austenite phase transition [3].

Ferromagnetic shape memory alloys (FSMAs) are actuated in the martensitic state in a magnetic field in which strains can be recovered when rotated about a magnetic field [4]. Therefore, FSMAs do not have to proceed through a phase transformation to recover the original shape. In 1996, Ullakko et al. found a 0.2% magnetic field induced strain (MFIS) in a Ni-Mn-Ga single crystal [5]. The MFIS of Ni-Mn-Ga single crystal increased

up to 6% in 2000 [6] and to 9.5% in 2002 by slightly varying the composition and martensite lattice modulations [4, 5, 7, 8].

Extensive research has been centered on bulk Ni-Mn-Ga to understand its mechanical and magnetic properties and phase transformation behavior. This system in bulk form is in general very brittle in polycrystalline state, making it difficult to deform into a desirable shape. Ductility can be improved in a single crystal or thin film form. Poly-crystalline thin films deposited with various physical vapor deposition (PVD) methods show superior mechanical properties [9].

Ni-Mn-Ga films can be fabricated by various deposition methods, the most commonly used being direct current (DC) and radio frequency (RF) magnetron sputtering [10], most often with a single alloyed target. When deposited at room temperature, Ni-Mn-Ga films are mostly nanocrystalline or even amorphous. The Ni-Mn-Ga film properties also depend on the choice of substrate material and substrates can be classified into three categories: single crystalline hard substrates; polycrystalline and amorphous hard substrate; and compliant substrates.

In-situ annealing while sputtering, sputtering with a heated substrate, impacts texture, grain size, structural ordering, and magnetic properties [11]. When grown on heated substrates and when annealed after deposition on cooled substrates, Ni-Mn-Ga films develop a strong 110 fiber texture [12]. Residual stress develops in film/substrate composites after cooling from elevated deposition temperatures or post annealing. The majority of stresses in thin films result from the interaction with the substrate. Origins are found in the thermo-elastic mismatch, difference of the thermal expansion coefficients,

densification processes in the film during deposition, during grain growth, and from phase transformations.

The martensite transformation temperature was found to increase for 14M martensite on Si(100) substrates [12] and the opposite trend was found for 10M martensite on Si(100) substrates [13].

CHAPTER 2: MOTIVATION

The focus of this thesis is on the development of a film deposition method using multiple sputter targets simultaneously to produce films and test the structural and magnetic properties of shape memory alloy films, specifically those of Ni-Mn-Ga. A large change in the mechanical properties occurs when the size of a piece is reduced, for example, film thickness relative to the characteristic length of a deformation mechanism [14].

Magnetic shape memory alloys (MSMAs), including Ni-Mn-Ga, exhibit a magnetic and structural coupling, which leads to large magnetic field induced strains of up to 10% in single crystal Ni-Mn-Ga [15-18]. Various levels of magnetically induced strains were reported for Ni-Mn-Ga films after removing the films from the substrate [19, 20].

Thin film deposition by DC and RF has emerged as the most common method of fabricating films [10]. Targeting specific compositions via sputtering has been accomplished using different techniques such as changing the single alloy target composition [21], adjusting deposition temperature [22], or varying sputter pressure [23]. Using a single alloy target proved difficult to vary composition accurately and a specifically designed target is needed for each desired composition range. Tri-sputtering deposition (sputtering with multiple targets simultaneously) offers more compositional

control as well as increased deposition rates, as multiple targets are used to deposit material.

The structural, thermal, magnetic, and mechanical properties of Ni-Mn-Ga depend strongly on composition. Accurate control of the composition is essential to achieve appropriate structural and magnetic transition temperatures. A robust procedure using three targets (Ni, Mn, and NiGa) is desirable for the compositional control needed to obtain Ni-Mn-Ga films with defined structural and magnetic properties.

The goal of this study is to sputter a 10M and 14M thin film by varying the power of three sputter source targets simultaneously to control film composition, and to characterize structural, microstructural, magnetic, and mechanical properties of these films.

CHAPTER 3: BACKGROUND

3.1 History

In 1903, German mining engineer, Friedrich Heusler described alloys that were ferromagnetic despite the fact that their constituent metals were not ferromagnetic [1]. In 1968, Rhyne et al. reported the permanent plastic deformation of Dy in a 10 T magnetic field [23]. It was Ullakko et al. who first reported a magnetic-field-induced strain in a Ni-Mn-Ga Heusler alloy [5]. This report triggered the development of other MSMA's and rapidly expanded MSMA research.

MSMA's like Ni-Mn-Ga tend to undergo a macroscopic shape change upon the application of an external magnetic field. The shape change is magnetoelastic if the MSMA returns to its original shape after the magnetic field is removed or magnetoplastic if the shape change is permanent. Magnetoplastic deformation is reversible, but it requires a magnetic field or mechanical stress to be applied perpendicular to the original magnetic field direction. Alternately, deformation may be achieved through either the application of a magnetic field or a mechanical stress. MSMA's only exhibit the magnetic shape memory effect in the martensite phase and below the martensitic phase transformation (as described in Section 3.3) temperature, which depends strongly on alloy stoichiometry.

3.2 Magnetism

Materials may be diamagnetic, paramagnetic, ferromagnetic, or antiferromagnetic. Ni-Mn-Ga MSMAs are ferromagnetic. All materials are influenced by

the presence of a magnetic field. Materials that are attracted to a magnetic field are considered paramagnetic, and have unpaired electrons. Materials that are repulsed by a magnetic field are diamagnetic, and have no unpaired electrons. Other materials have a more complex relationship with an applied magnetic field such as ferromagnetism and antiferromagnetism.

In a solid material, the sum of the magnetic moments of all atoms provides a macroscopic magnetic moment per unit volume, called magnetization, M. A magnetic field can be described by a magnetic field induction, B, and the magnetic field intensity, H, which are related through the permeability of free space, μ_0, and in a material all are related through [24, 25].

$$B = \mu_0(H + M) \tag{1}$$

The magnetization and magnetic field of a material are related through the magnetic susceptibility, χ.

$$M = \chi H \tag{2}$$

The magnetic susceptibility is either positive for paramagnetic materials or negative for diamagnetic materials.

3.2.1 Paramagnetism

Paramagnetic materials have magnetic dipoles. A magnetic dipole is a closed circulation of electric current due to the spin of unpaired electrons in atomic or molecular electron orbitals [25]. Thermal energy causes the dipoles to be randomly oriented. The random orientation results in zero net magnetization. In a magnetic field, the dipoles are free to rotate and tend to align parallel to the applied field (Figure 3.1). The magnetic

susceptibility of paramagnetic materials is small and positive in a magnetic field (Figure 3.2). Paramagnetism is also temperature dependent. At higher temperatures, thermal motion, or entropy, competes with the tendency for dipoles to align with the magnetic field, leading to a reduction of the magnetic susceptibility. For low levels of magnetization, as seen in paramagnetism, Curie's law:

$$\boldsymbol{M} = \chi\boldsymbol{H} = \boldsymbol{H}\,\frac{C}{T} \tag{3}$$

T is absolute temperature measured in Kelvins, and C is a material-specific Curie constant. Curie's Law indicates that the susceptibility of the material is inversely proportional to their temperature [25].

In metals, free electrons contribute to the so-called Pauli paramagnetism.
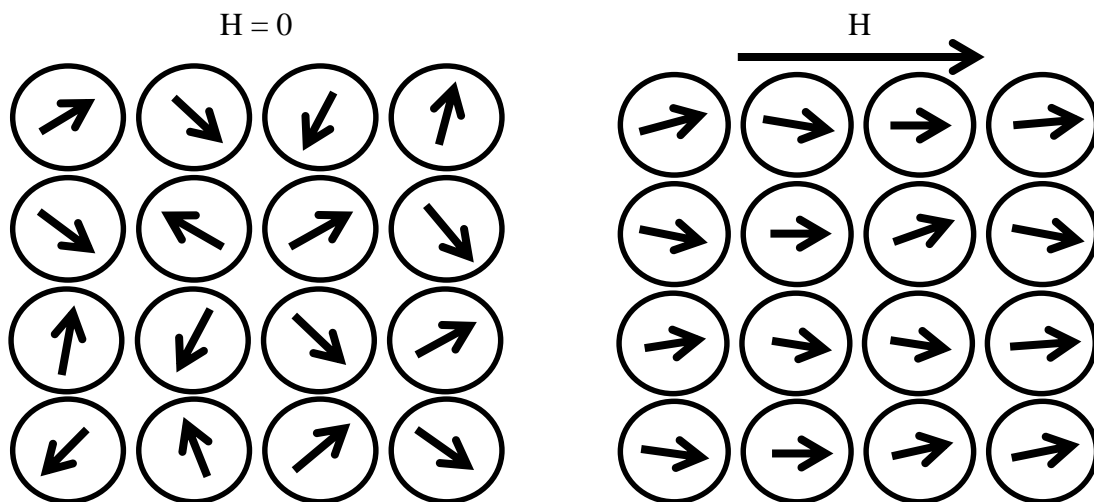
Figure 3.1: **Paramagnetic atomic dipoles without (Left) and with (Right) a magnetic field applied.**
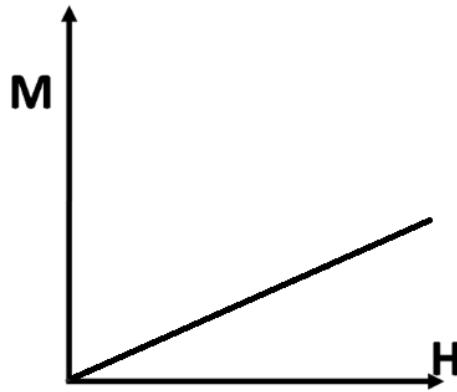
Figure 3.2: **Magnetization versus applied field graph of a paramagnetic material shows a positive susceptibility, Equation 2. A saturation behavior at high magnetic fields can occur (not shown, see Figure 3.5).**

3.2.2 Diamagnetism

Diamagnetism is a quantum mechanical effect that occurs in all materials, where it is the only contribution of magnetism in the material and is nonpermanent with a negative magnetic susceptibility [25]. Diamagnetic materials do not have a magnetic moment because there are no unpaired electrons to contribute to the net magnetic moment. In an applied magnetic field, the orbital motion of the electrons is changed and a magnetic moment is induced. The induced magnetic moment orients opposite the applied field (Figure 3.3) following Lenz's law:

$$\varepsilon = -\frac{\partial \Phi}{\partial t} \qquad (4)$$

which indicates that the induced voltage, ε, and the change in magnetic flux, Φ, have opposite signs [25].

H = 0   H
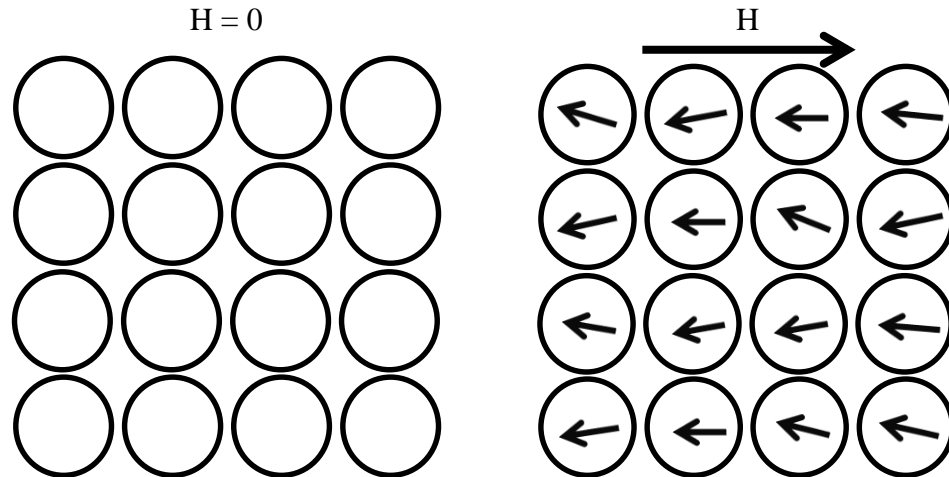
Figure 3.3:   Diamagnetic atomic dipoles without (Left) and with (Right) a magnetic field applied.

The magnetic susceptibility is small, negative (Figure 3.4), and independent of

temperature. The negative susceptibility is due to the induction phenomenon which

reduces the applied magnetic field effects according to Lenz's Law.
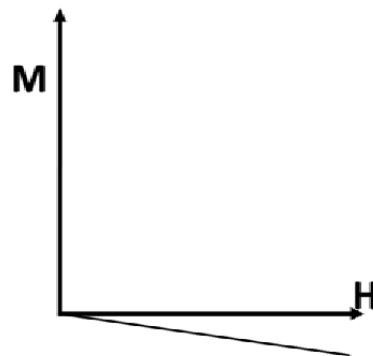
Figure 3.4:   Diamagnetic materials have a negative magnetic susceptibility.

3.2.3 Ferromagnetism

Ferromagnetism occurs in materials where the atoms have unpaired electrons and

magnetic moments of neighboring atoms couple. Neighboring magnetic moments can

couple parallel to each other (ferromagnetic) or couple anti-parallel (antiferromagnetic). Neighboring magnetic dipoles align parallel or anti-parallel to lower the energy of the system [25].

Magnetic moments align in volumetric regions in a material. A volume of uniformly aligned moments is called a domain. Domains can orient randomly throughout the sample such that the net magnetization cancels. In a magnetic field, the domains that are aligned with the applied magnetic field direction begin to grow at the expense of the other domains. Figure 3.5 shows the change in magnetic domains as the applied field is increased. As the magnetic field increases, the domains more parallel to the direction of the applied magnetic field grow. Finally, the magnetic moments rotate parallel to the applied field and magnetization saturates. When the applied field is removed, the domains can maintain the alignment and the magnetism remains. This means that ferromagnetic materials can remember their past magnetic history.
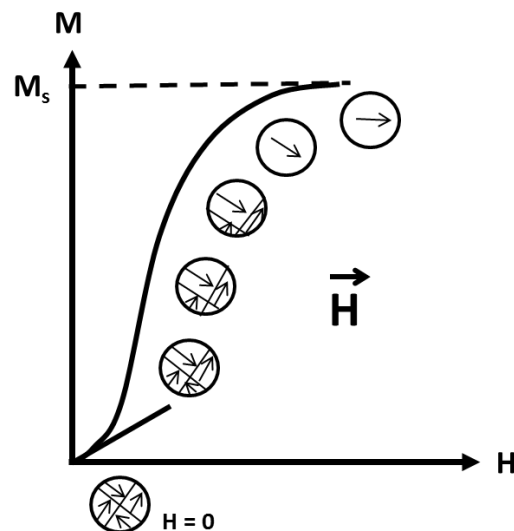
Figure 3.5:   The change in magnetization with increasing field strength. The dashed line is the saturation magnetization, where all magnetic domains are fully aligned with the field.

Figure 3.6 shows a magnetization hysteresis. When the applied magnetic field is reduced to zero after magnetic saturation (Figure 3.6 (c)), a residual magnetization may remain due to magnetic domains that are still aligned in the direction of the applied magnetic field. The residual magnetization is called the magnetic remanence. As the applied magnetic field increases in the opposite direction, the magnetization will reach zero (Figure 3.6 (d)), due to the cancelation of the magnetic moments over all domains. This zero magnetization value is the field necessary to remove all magnetization, and is called the negative coercive field strength. Increasing the applied magnetic field in the opposite (negative) direction will result in all of the magnetic domains aligning with the negative field, reaching saturation magnetization again (Figure 3.6 (e)). When the field is increased to zero, some of the domains will remain aligned and the magnetization reaches negative remanence (Figure 3.6 (f)). With increasing magnetic field strength in the positive direction, the magnetization reaches zero at the positive coercive field (Figure 3.6 (g)). Upon a further increase of the magnetic field in the positive direction, the material will again reach saturation magnetization.

As temperature increases, entropy energy competes with magnetic exchange energy and causes second order magnetic transitions. When the temperature rises beyond a critical value, the Curie temperature or T_c, the sample turns paramagnetic (Figure 3.7).
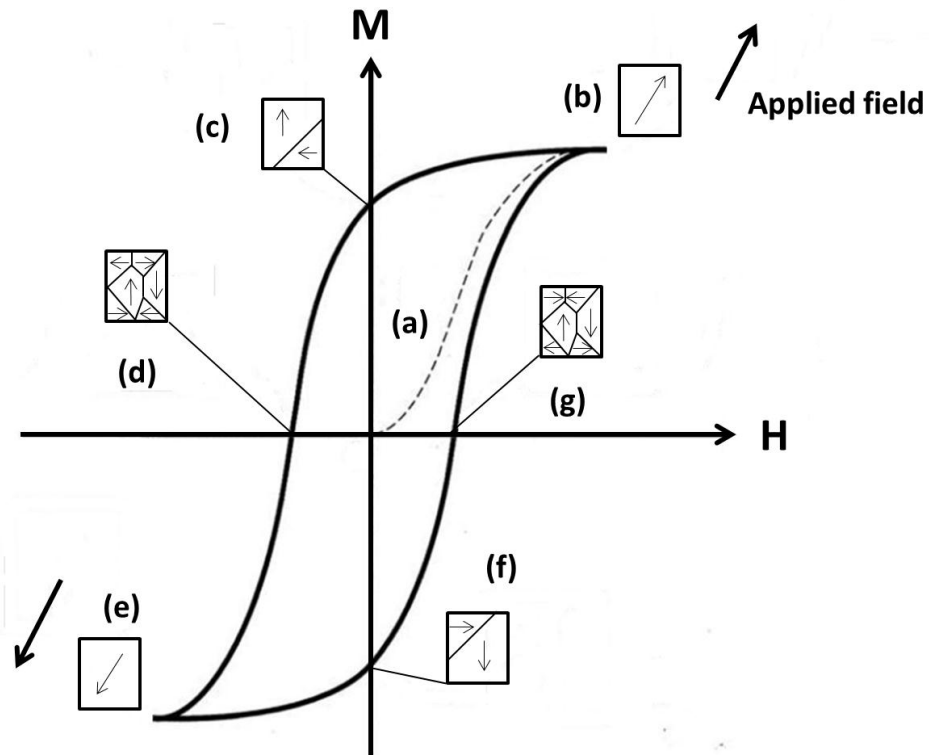
Figure 3.6: Schematic of a magnetization hysteresis of a ferromagnetic material. (a) is the initial magnetization curve (virgin curve) to saturation magnetization, (b). (c) shows the positive remanence, and (f) the negative remanence. The negative coercive field and positive coercive field are at points (d) and (g), respectively. At (e), the material has reached negative saturation magnetization. The small insets at each point illustrate the magnetic domain directions relative to the applied field direction.
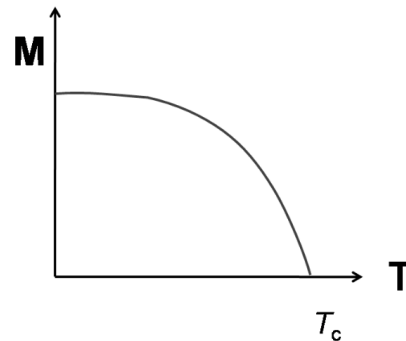
Figure 3.7: Temperature dependence of saturation magnetization. The saturation magnetization decreases as temperature increases and vanishes at the Curie temperature, T_C.

3.3 Heusler Alloys

The Heusler $L2_1$ type structure may be conveniently considered as four interpenetrating f.c.c. sublattices [26, 27]. For Ni_2MnGa, nickel atoms occupy sites (¼, ¼, ¼) and (¼, ¼, ¾), while manganese and gallium occupy sites (½, 0, 0) and (0, 0, 0) respectively (Figure 3.8).
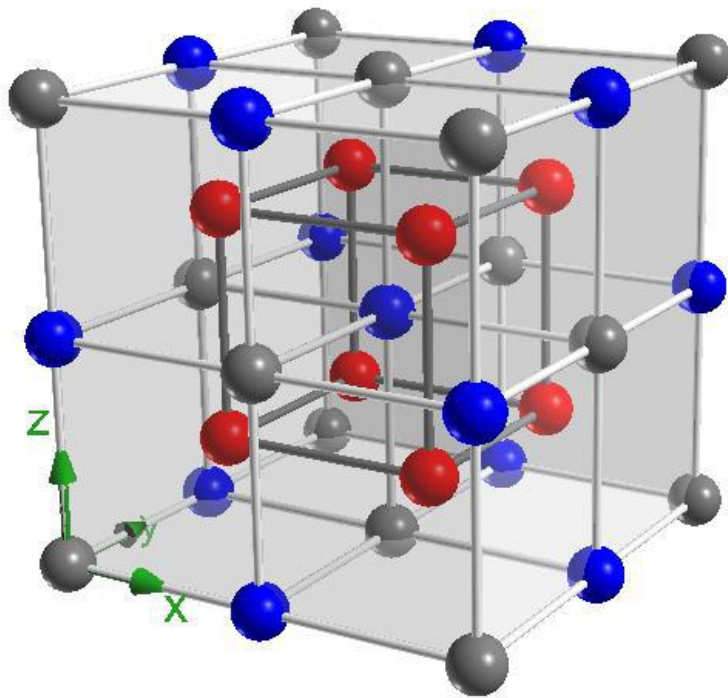
Figure 3.8:   Crystal structure Ni_2MnGa Heusler phase, modified from [13]. Ni atoms are represented by red, Mn atoms by blue, Ga atoms by grey.

In the $L2_1$ structure, the electrons of the manganese atoms couple through a double exchange mechanism to create ferromagnetic ordering. The double-exchange mechanism is a type of a magnetic exchange that may arise between two species, and has important implications for whether materials are ferromagnetic or antiferromagnetic. The double-exchange theory predicts that an electron couples between neighboring

manganese atoms via intermittent nickel and gallium atoms. The movement from one species to another and the distance of the electron jump drives the magnetic moment that is induced [28]. The resulting magnetic moment from manganese is one order of magnitude larger than that of the contribution from nickel atoms. The magnetic coupling is driven by the manganese atom spacing [26, 28, 29]. However, manganese is generally antiferromagnetic; the change from antiferromagnetic behavior to ferromagnetic behavior is due to the increase in distance between the manganese sites compared to the distance between manganese atoms in a pure manganese lattice. The increased interatomic distance changes the Mn-Mn exchange interaction from antiferromagnetic to ferromagnetic [26]. Table 3.1 lists the magnetic properties of a Ni_2MnGa Heusler alloy.

The total magnetic moment is the stoichiometric sum of each species magnetic moment. Since the ferromagnetism of Ni-Mn-Ga is due to manganese locations in the lattice [26], off-stoichiometric compositions can lead to the excess manganese atoms coupling antiferromagnetically. Because the magnetic moment of manganese is much larger compared to those of nickel and gallium, the total magnetic moment is determined by manganese

Table 3.1: **The magnetic moments of Ni_2MnGa and its constituent atoms. μ_{total} is the total theoretical saturation moment with the experimental value in parenthesis. μ_i are the spin magnetic moments of each species [27].**

	μ_{total} [μ_B]	μ_i [μ_B]	
Ni_2MnGa		Ni	0.37
	4.09 (4.17)	Mn	3.36
		Ga	-0.04

3.4 Martensitic Transformation

Martensitic phase transformations are an important phenomenon in shape memory alloys [30]. Martensite refers to a crystal structure that is formed through a displacement transformation. The martensitic phase transformation is a diffusionless transformation [30, 31]. Ferromagnetic shape memory alloys like Ni-Mn-Ga undergo a martensitic phase transformation.

Pons et al. [31] have identified the crystal structures of the different martensites observed in Ni-Mn-Ga alloys below the martensite transformation temperature. The different structures depend on composition, temperature, and mechanical stress. There are three common structures, a five-layered modulation (10M, Figure3.9 (b)), a seven-layered modulation (14M, Figure3.9 (c)), and non-modulated (NM) [31]. The "M" in 10M and 14M stands for monoclinic. The electronic concentration (electrons per atom), e/a, plays an important role in stabilizing the Heusler structure and defining the magnetic order and structural phase transformation in Ni_2MnGa [27]. The electron concentration can account for the different martensite lattice modulations in Ni-Mn-Ga alloys [32]. Lanska et al. [33] and Richard et al. [34] found a general trend in the structures of the martensite phase in Ni-Mn-Ga samples that were related to the e/a ratio. In Lanska et al., an increasing e/a resulted in a progression from 10M to 14M to NM. Richard et al. show the change from 10M to 14M solely depends on the Ni/Mn ratio.

The martensitic phase transformation of Ni-Mn-Ga Heusler alloys occurs between the high symmetry, high temperature cubic austenite phase and the low symmetry, low temperature martensite phase. The martensitic phase transformation exhibits a temperature hysteresis. Upon cooling, the phase transformation begins at the martensite

start temperature, M_s, which is below the equilibrium temperature and ends at the

martensite finish temperature, M_f. Upon heating, the transforming is reversed, martensite

into austenite. The reverse transformation begins at the austenite start temperature, A_s,

which is above the equilibrium temperature and ends at the austenite finish temperature,

A_f.
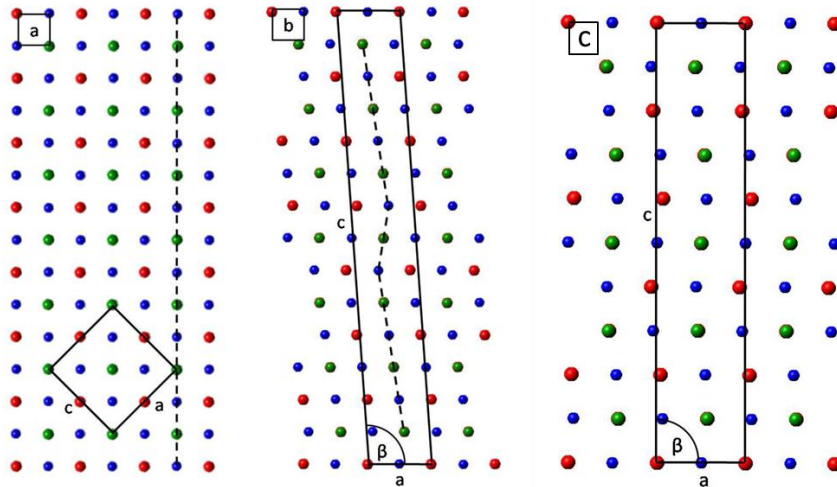
Figure 3.9: **Crystal structure of the (a) cubic austenite phase, (b) 14M martensite structure, and (c) 10M martensite structure, represented as a body-centered monoclinic unit cell. The stacking sequence is emphasized by dashed lines. Gallium occupies red sites, manganese green, and nickel blue.**

The composition dependence of the martensitic transformation temperature has

been studied in detail [31, 35]. These studies observed a variation of M_s from 154 K to

458 K, from a variation of elements within 5 atomic percent.

In stoichiometric Ni_2MnGa the martensitic transformation temperature is -118 °C

[35]. Off-stoichiometric compositions like $Ni_{50} Mn_{30} Ga_{20}$ (atomic percent), allow the

martensitic phase transformation temperature to occur at approximately 28-52 °C [34].

Chernenko et al. [31] concluded that:

- At a constant manganese content, addition of gallium lowers M_s

- Addition of manganese, instead of gallium, at a constant nickel concentration increases M_s.

Substitution of nickel by manganese, at constant gallium, results in alloys with lower M_s.

3.5 Thin Film Mechanics

When a body is subjected to an external force, internal forces develop. Mechanics deals with the behavior of solid bodies when they are subjected to a variety of different loading conditions where stress is induced. Ohring suggested that even if classical mechanics solutions were relevant, other factors affect the mechanical behavior and must be considered [36]:

1. Virtually all films on a substrate are stressed, even without the application of a load extended to the film/substrate system.
2. The mechanical behavior of a thin film cannot be considered separate from the substrate.
3. The miniscule dimensions of the stressed components must be considered.

The mechanical behavior of films is strongly influenced by average grain size, grain shape, and crystallographic texture [37]. Also, the crystalline anisotropy of thermal and mechanical properties has a more pronounced effect on the overall mechanical behavior of films. One way to estimate the stress in a film is through its effect on substrate curvature. The Stoney equation describes the relationship between substrate curvature and the in-plane stress in a film [38].

$$\sigma_f = \frac{M_{ss}d_s^2}{6Rd_f} \tag{5}$$

The Stoney equation relates the in-plane film stress to the substrate curvature, $k=1/R$, the film and substrate thicknesses, d_f and d_s, respectively, and the biaxial modulus of the substrate $M_{ss} = \frac{E_{ss}}{1-v_s}$. The Stoney equation does not contain any elastic parameters of the film. Thus, the Stoney equation provides a means to determine the film stress from the radius of substrate curvature if the elastic parameters of the substrate are known.

3.6 Sputtering

Sputtering is a physical process where atoms are ejected from a solid target material through a momentum transfer of incident ions. Sputtering is a non-thermal process and the target is continually cooled below room temperature. The target material is connected to a negative voltage for DC or RF sputtering.

The simplest sputtering configuration is DC diode sputtering. First gaseous plasma is created over the source material ("target"). The target is negatively biased to accelerate the ions from the plasma into the target. During the ion bombardment of the target, the surface atoms are ejected from the target. The ejected atoms are deposited onto all objects in the sputtering chamber.

DC-magnetron sputtering incorporates a magnetic field over the target via magnets positioned between the gun and target material. The magnetic field confines charged plasma particles in isolated orbits, greatly increasing the probability of ion target interaction. An increase in the number of incident ions or increase in their incident energy increases the sputter yield (i.e., the number of sputtered atoms per incident ion). Also by

trapping the ions within the plasma, the pressure required to sustain the plasma is much lower. The sputtered atoms are neutral and are unaffected by the magnetic trap. DC and DC-magnetron sputtering functions only with conductive materials as targets.

RF sputtering overcomes limitations of the DC mode. RF sputtering can be applied to non-conducting oxides and other insulating materials. The RF mode works by varying the sign of the anode-cathode bias at a high frequency (commonly 13.56 MHz) [39]. RF has greatly extended the versatility of sputtering.

Sputtering offers many advantages over evaporative or chemical vapor deposition. For evaporative deposition, each element requires different vapor pressures and melting temperatures. Deposition via evaporation when multiple elements are needed can be difficult or impossible for multi-component systems. Evaporative deposition can lead to poor stoichiometry control and requires a controlled high vacuum throughout the deposition process, greatly reducing the adjustability of the process. Sputtering also has better substrate adhesion, lower sputtering temperatures and thickness uniformity over large planar areas, as opposed to the evaporative process.

3.7 Texture

The crystallographic texture of a material is the distribution of grain orientations. The texture of a polycrystalline film may be influenced by a variety of factors including deposition method, substrate material, geometry, or surface features. Texture can either show crystallographic orientations of no preference relative to the sample, which is referred to a random texture, or a preferred orientation relative to the sample. Fiber texture is a "Range of orientations limited to a single degree of rotational freedom about a fixed axis" [39]. In spherical texture, all crystallographic axes can have preferred

orientation. Random texture has no preferred orientation. X-ray diffraction allows the measurement of the extent of the crystallographic texture in a film and can be mapped in a stereographic projection.

CHAPTER 4: EXPERIMENTAL

4.1 Characterization of Sputter Deposition System

The sputter deposition system was characterized for sputter rate using a single alloy target with composition $Ni_{37.75}Mn_{36}Ga_{26.25}$ atomic percent, by varying the sputter parameters: power to target: 25, 50, 75, and 100 Watts, argon pressure: 3 mTorr, and 8 mTorr, and working distance (distance from target to substrate): 30, 40, and 50 (distances are arbitrary indicator marks and are approximately in the range of 5 cm to 15 cm with the 50 mark correlating to the 5 cm distance). A maximum of 100 W for the nickel and nickel-gallium targets and 50 W for the manganese target were used in an attempt to reduce target failure associated with higher powers. Equipment limited the lowest working argon pressure to 3 mTorr. A high deposition temperature was used with the aim of in-situ annealing. Previous experiments were successful in obtaining chemically and magnetically ordered films without post-deposition thermal treatment. The films were deposited on a heated, 500º C single crystalline silicon (100) wafer with a native oxide layer. The sputtering parameters of argon pressure, substrate temperature, working distance, and time were held constant at 3 mTorr, 500 °C, 40 (approximately 10 cm) and 60 minutes respectively, after characterization was complete.

4.2 Ni, Mn, Ni-Ga

A target of pure gallium could not be used because gallium is liquid at the operating temperatures required for sputtering. Instead a target composition of $Ni_{50}Ga_{50}$

was chosen because it maximized the amount of gallium in the target that we could successfully produce. The Ni-Ga target [Ni (99.9%, ESPI Metals, Ashland, OR), and Ga (99.9999 %, Atlantic Metals & Alloys, Stratford, CT)] was produced by drop casting.

The nickel and gallium elements were weighed to a 0.01 g precision for a total target mass of 61.04 g, yielding an accuracy of 0.05 atomic percent. The weighed material was placed in a high purity fused alumina crucible, which was inserted into a high quality fused quartz tube. The stacked crucible assembly was evacuated with a turbo pump to approximately 7.0×10^{-4} mbar, purged and backfilled with argon to atmospheric pressure and sealed (Figure 4.1). The quartz tube protected the furnace from the molten alloy in the event a crack developed in the alumina during heating or cooling. The sealed assembly was loaded into a Reitel Induret Compact induction furnace (Figure 4.2) and pre-melted at approximately 1250 °C. The temperature was held constant for two minutes, and cooled to 25 °C. The cooled alloy nugget was crushed using a die and press, then sifted through a #10 testing sieve to ensure uniform material distribution for the second melting process. The Ni-Ga powder was placed in an alumina crucible with a plunger stop inserted (Figure 4.3), and then placed in the upper chamber of the casting furnace. The casting furnace was sealed and evacuated using a Venturi vacuum system to a pressure of -1 bar. The system was purged with high purity argon to 2 bar and re-evacuated. This process was performed five times to minimize the oxygen partial pressure. The material was inductively heated to 1250 °C and drop cast into a copper mold (Figure 4.4) that was 5.38 cm in diameter and 0.318 cm thick. An oversized mold diameter was used to obtain a 2 inch target, compensating for material shrinkage during cooling. Immediately after casting, the target was removed from the mold and placed into

an 800 °C table top box furnace. The temperature was reduced discontinuously in steps of

200 °C. The furnace temperature was held constant for 24 hours at 800 °C, 600 °C,

400 °C, and 200 °C. The post-cast annealing was needed to relieve stress in the target

developed during casting that would otherwise cause catastrophic target failure.
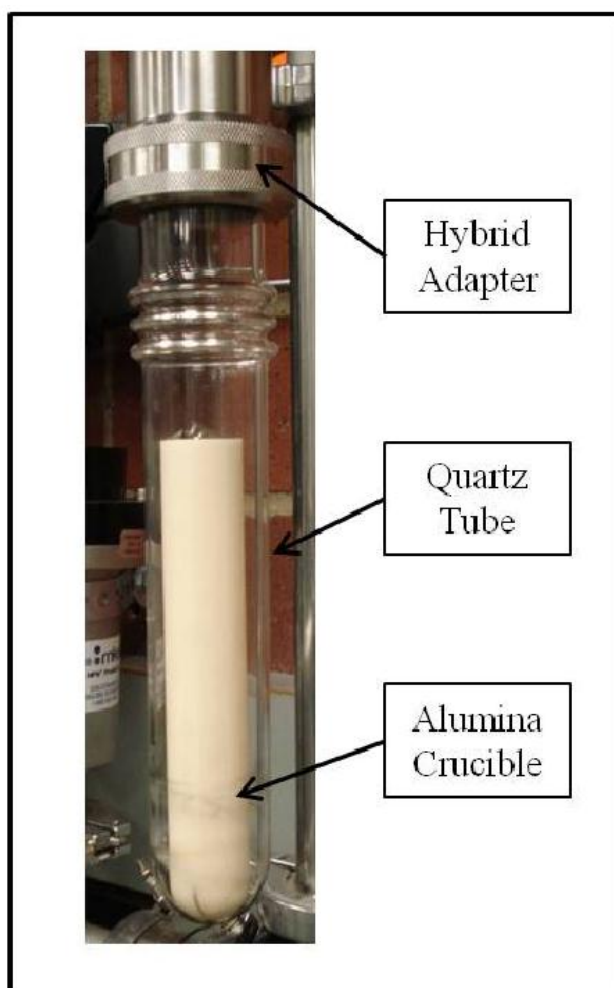
Figure 4.1:   Crucible assembly showing the alumina crucible inside the quartz tube and clamped by the hybrid tube adapter attached to the vacuum pump.
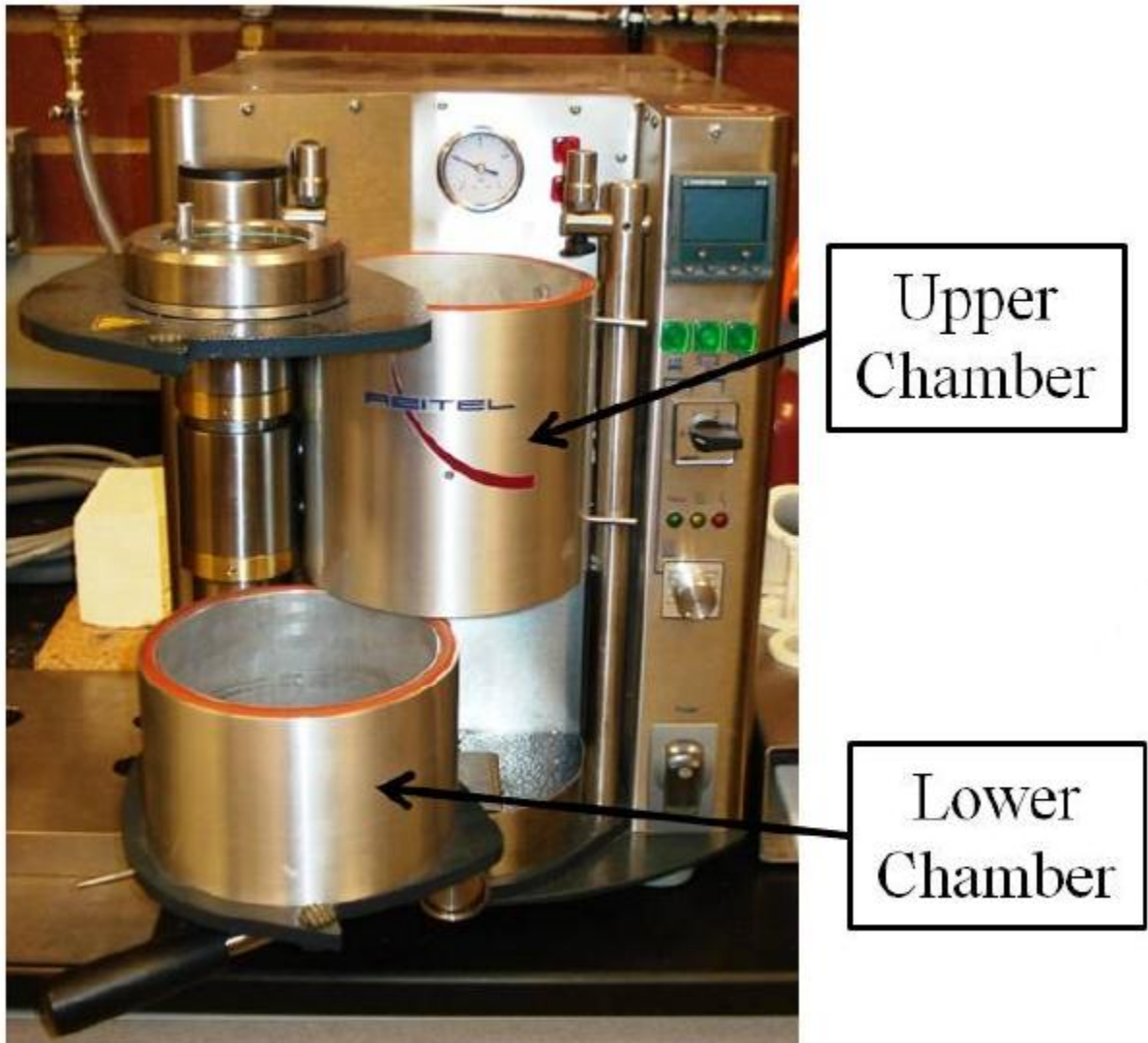
Figure 4.2: Reitel induction furnace. Modifications to the safety lockout attached to the upper chamber cover were made to allow the furnace to operate while the upper chamber cover is in the open position. The target mold sits in the lower chamber.

Figure 4.3:   Alumina crucible and stopper used to melt NiGa powder prior to casting

Figure 4.4:   Copper mold used to cast NiGa target

4.3 Sputter Deposition

A design of experiment (DOE) was completed to obtain the sputtering characteristics of the three targets for tri-deposition in the sputter tool. The DOE consisted of 9 variations of gun power settings. The nickel and nickel-gallium target powers used were, 100 W, 50 W, 30 W, and 15 W. The manganese target was limited to a maximum of 50 W due to its low thermal conductance and the powers used were, 50 W, 30 W, and 15 W. The DOE resulted in a composition map of possible compositions from varying only gun power to each target.

The films were sputtered with a ATC 2000 UHV five two inch target magnetron sputtering system (AJA International, Figure 4.5). The system had two 750 W DC power supplies, two 300 W RF and a 100 W RF bias/etch power supply. A Pfeiffer HiPace 80 turbomolecular drag pump was used to evacuate the load lock chamber to a pressure of approximately 10^{-6} Torr. A Pfeiffer HiPace 300 turbomolecular drag pump was used to evacuate the main sputter chamber to a base pressure of 10^{-7} Torr. While sputtering, the substrate chuck was rotated and elevated substrate temperatures were possible via a quartz halogen lamp heater. Ultra-high purity argon (99.999%) was used as the inert gas, with a sputtering working pressure between 3 mTorr and 30 mTorr.

Sputter rates depend on sputtering power, working distance, and chamber pressure. Three targets (Nickel, Manganese, Nickel-Gallium) with a 2 inch diameter, including two commercial element targets with 99.9% Ni (Kurt J. Lesker, Clairton, PA) and 99.9% Mn (Process Materials, Livermore, CA) and one alloy target with 50 at.-% Ni and 50 at.-% Ga, served as the material sources for sputtering the Ni-Mn-Ga films.

The three targets were positioned as in Figure 4.6. The nickel and nickel-gallium targets were loaded on DC magnetron guns. The manganese target was loaded on the RF magnetron gun. The substrate was loaded into the sputter chamber via a load lock chamber and loaded onto a rotational chuck. Once the chuck height (working distance) was set, the chamber was raised to a pressure of 30 mTorr. The guns and target were powered to, Ni: 10 W, Mn: 10 W and NiGa: 12 W, to strike the plasma and the substrate was ramped to 500 °C at 100 °C/min. After the substrate reached 500 °C, temperature was held constant while the guns and targets were raised to the desired wattage over 5 minutes. A high deposition temperature of 500 °C was used to in-situ anneal during film deposition, based on previous experiments. Once the desired power was reached, the shutter lid to each target chimney was opened for the designated coat time. During sputtering, the deposition rate was monitored with an INFICON SQM-160 rate/thickness monitor. Once the desired sputter time was reached, the shutter lid was closed and the power was ramped down to zero over 5 minutes. The substrate was cooled to 30 °C at a rate of 14 °C/min and removed from the sputter chamber via the load lock. Table 4.1 lists the power, voltage, and amperage for each gun during a sputtering session for the targeted $Ni_{50}Mn_{30}Ga_{20}$ composition. Refer to Table 5.3 for all sputter experiments.

Table 4.1:   Example of the power supply conditions during a sputtering process

Target	Gun Type	Power [W]	Voltage [V]	Amperage [mA]
Ni	DC	30	320	92
Mn	RF	50	216	-
NiGa	DC	30	346	85
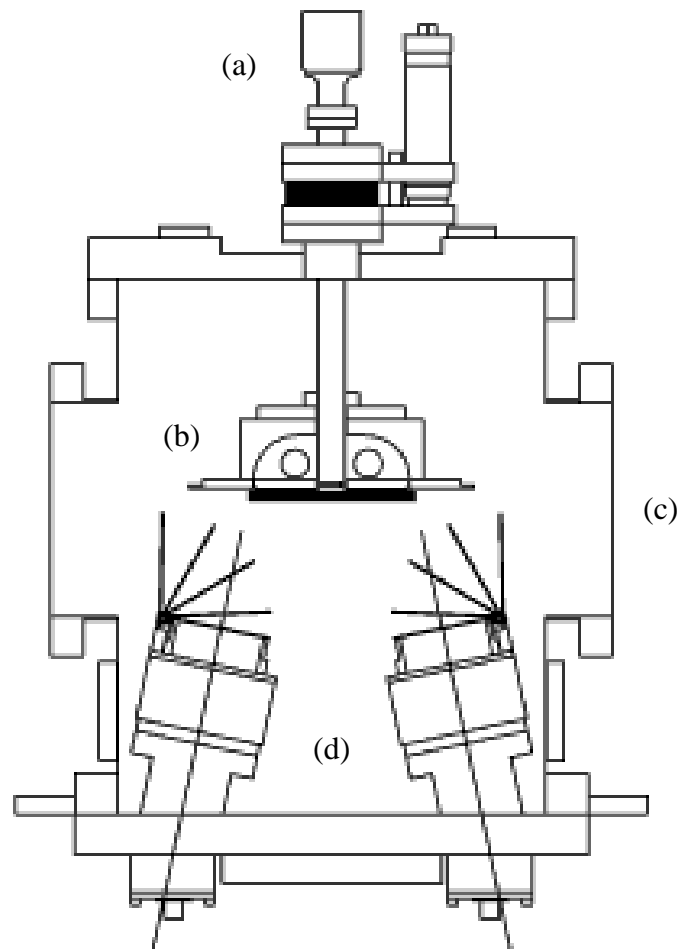
Figure 4.5: Side view of sputter system cross section from AJA International (www.ajaint.com). (a) is the substrate rotation motor and working distance adjustment. (b) is the substrate chuck with heater assembly and substrate. (c) is the sputter chamber. (d) are two of the sputter gun, target, chimney, and lid assemblies.

Wall

(MM) – Magnetic Material
(MR) – Maximum Rate

(Gun #1) DC 1
(MM)

Ni

(Gun #5) DC 5B
(MR)

(Gun #2) RF 2
(MR)

Mn

NiGa

(Gun #4) RF 3
(MR)

(Gun #3) DC 5A
(MM)

Front of the Machine
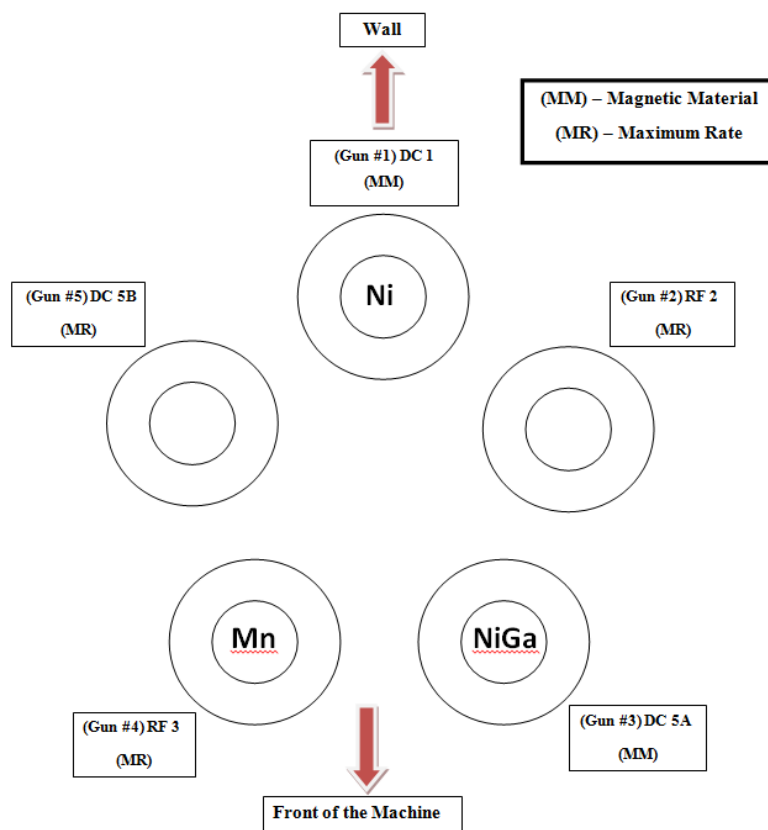
Figure 4.6: Sputter tool gun and target layout. The targets were spread as evenly in the chamber as possible. Each DC-magnetron gun can have the magnetic field set up for maximum rate or basic magnetic material mode. It is possible to load and use 5 targets, but 3 simultaneously.

4.4 Energy-Dispersive X-ray Spectroscopy

Energy-dispersive X-ray spectroscopy (EDS) is an analytical technique for the determining the chemical composition of a sample. It relies on the electron beam interaction with a sample and the x-ray excitation associated with the electron interaction. A photon from the incident beam is absorbed by an inner orbital electron, which displaces the electron, allowing an outer orbital electron to relax and fill the vacancy. The relaxation process results in a decrease in electron energy and the energy difference (i.e., difference between the outer and inner energy orbital) is released as an x-ray photon. Because the energy difference between the outer and inner orbitals depends on the

element in which they exist, the x-ray is characteristic to the element from which it was released.

A spectrum of the energy versus relative counts of the detected x-rays was obtained and evaluated for qualitative and quantitative determinations of the elements present in the sampled volume. Accuracy depends on the detector type, interaction volume, and the frequency of x-rays.

The composition of the sputtered films were analyzed with a Hitachi S-3400N-II Analytical Scanning Electron Microscope (SEM) equipped with an Oxford Instruments EDS package. Data was collected with an accelerating voltage of 20 kV, a probe current of 76.1, and a working distance of 10 mm. This system had a spatial resolution of 3 nm and detection limit of 0.1 atomic percent (at %). A 99.999% nickel standard was used to calibrate the beam before composition scans were taken. The scan was taken over a 5 mm x 5 mm sample from the center of the sputtered film.

4.5 Vibrating Sample Magnetometer

The Vibrating Sample Magnetometer (VSM) operates based the physics principles described by Faraday's Law of Induction, which states that a changing magnetic field will produce an electric field. The VSM measures the voltage induced in the pick-up coils to determine the magnetization of a sample. The sample is placed in a constant magnetic field. In a constant magnetic field, the magnetic domains will align in the direction of the applied field. The larger the applied field, the larger the magnetization. The magnetic dipole moments create a magnetic field around the sample. As the sample is vibrated, the magnetic stray field from vibrating the sample changes as a function of time and can be sensed by a set of pick-up coils. The alternating magnetic

field caused a voltage in the pick-up coils according to Faraday's Law. The voltage is proportional to the magnetization of the sample. By slowly changing the external magnetic field, magnetic hysteresis is measured.

Magnetization measurements were performed using a ADE (now MicroSence) Model 10 Vibrating Sample Magnetometer (VSM, Figure 4.7). The VSM consisted of four systems: an electromagnet, vibrator and sample holder, power supply with current reversing switch, and lock-in amplifiers with computer. For all magnetization measurements preformed, the pole gap was set at 40 mm. The electromagnet could be rotated 360 degrees around a vertical axis.

The VSM was equipped with a Model 3474-140 electromagnet manufactured by GMW magnet systems, capable of generating a 2 Tesla magnetic field.

The electromagnet was powered by a Xantrex model 80-150 power supply capable of providing 150 amps at 80 V. The power supply was fitted with a GPIB interface that was controlled by a computer. The polarity of the current to the electromagnet was reversed using a GMW model 5970-160 solid state current reversing switch. The current reversing switch was also fitted with a GPIB interface and was controlled by a computer to switch the current polarity as necessary.

The sample resided in a column containing eight pick-up coils (four x-coils and four y-coils). A speaker coil operating at 75 Hz introduced an axial motion through the sample holder perpendicular to the magnetic field. Lock-in amplifiers magnified the pick-up coils signals and filtered out the 75 Hz introduced by the vibrator. A resistive coil heater heated the sample to 180 °C. Cold N_2 gas was blown across the sample to cool it to -100 °C.

The VSM was used to measure saturation magnetization and characterize the Curie temperature of sputtered Ni-Mn-Ga films. A film was attached to a quartz sample rod and positioned between the pick-up coils. The magnetic field was increased to 2 Tesla (T) and returned to zero field while recording film magnetization. The magnetic field was then raised to 2 T and a hysteresis loop from +2 T to -2 T was performed. The Curie temperature measurements were performed in a low magnetic field to characterize the martensite to austenite phase transformation. Each sample had a size of approximately 5 mm x 5 mm. Once placed in the VSM, a static magnetic field of 250 Oe (0.025 T) was applied. The sample was then heated from -40 °C to 100 °C at a rate of 4 °C/min. After reaching 100 °C, the film was cooled back to -40 °C at a rate of 4 °C/min.
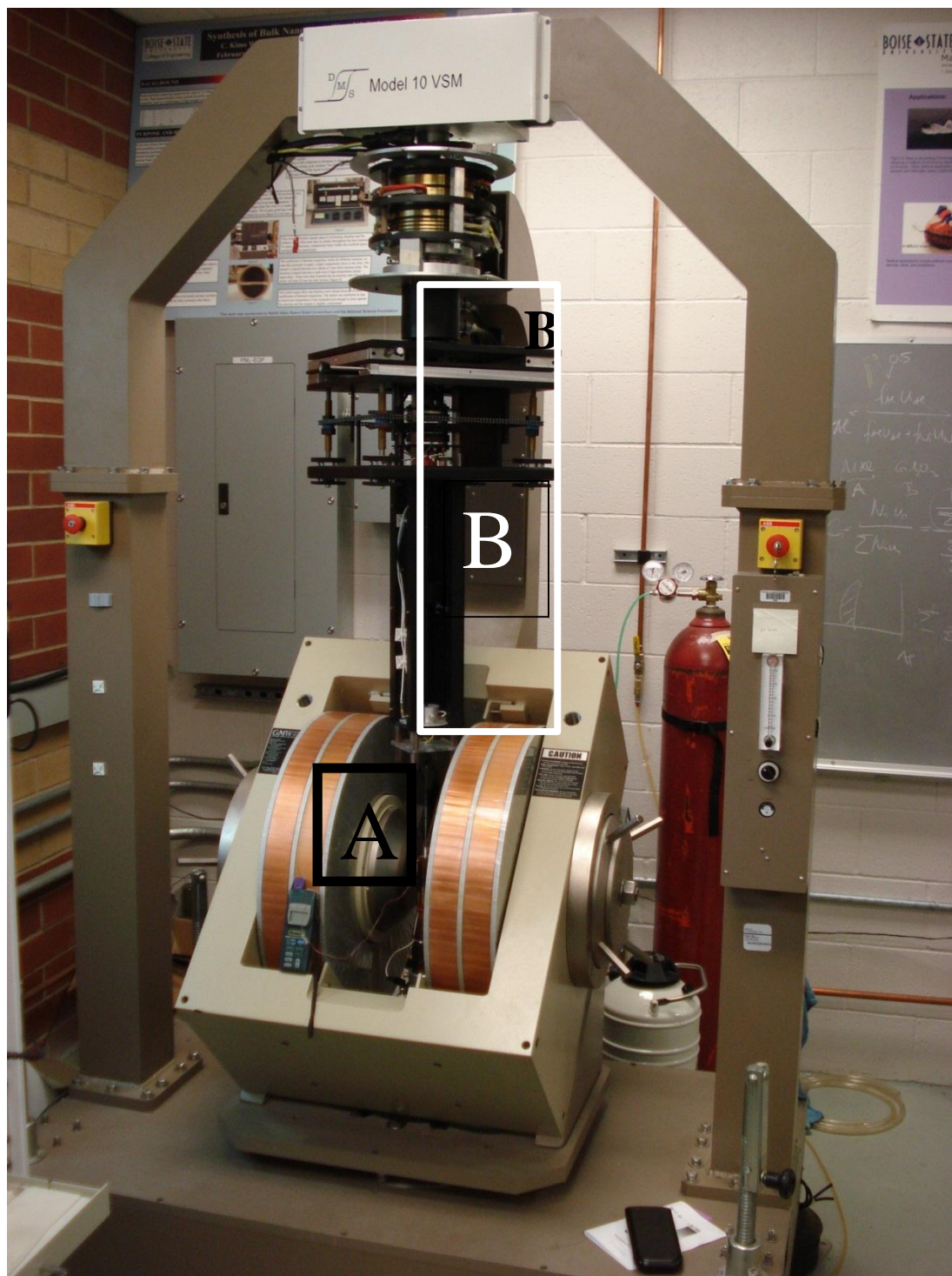
Figure 4.7:   VSM with A) electromagnets and B) sample holder and vibrator assembly

4.6 Wafer Curvature Deflectometery

A multi-beam optical sensor (MOS) thermal scan wafer bow measurement tool (k-Space, Ann Arbor, Michigan, Figure 4.8) was used to measure the change in curvature of the film-substrate composite. The stress in a thin film is related to the curvature in the film-substrate composite as previously described. By rearranging Equation 5, a relationship for the change in curvature is:

$$\kappa - \kappa_0 = \frac{6\sigma_f h_f}{M_{ss} h_s^2} \tag{6}$$

where κ is the stress-induced curvature of the substrate, κ_0 is the curvature of the substrate with zero film stress, σ_f is the biaxial, in-plane film stress, h_f and h_s are the film and substrate thicknesses respectively, and M_{ss} is the biaxial elastic modulus of the substrate.

A MOS uses a two-dimensional array of low energy lasers to measure the relative curvature of a film on a substrate. The film curvature changes the distance between the two-dimensional laser array spots. The change in array spot distance corresponded to a change in curvature as:

$$\Delta\kappa = \frac{1}{\rho} = \frac{\cos\phi_R}{2L}\left[1 - \frac{\Delta D}{D_0}\right] \tag{7}$$

where ϕ_R is the angle of reflection of the laser array, L is the length between the sample and the CCD camera, D is the average spacing between beams in the array, D_0 is the average initial spacing, ρ is the radius of curvature of the film, and κ is the film curvature.

A change in temperature, ΔT, and the mismatch of thermal expansion coefficients, $\Delta\alpha$, between the film and substrate causing a strain change, which caused the biaxial stress to change as:

$$\Delta\sigma_f = M_f\Delta\alpha\Delta T \;\Rightarrow\; \frac{\Delta\sigma_f}{\Delta T} = M_f\Delta\alpha \tag{8}$$

where M_f is the biaxial elastic modulus of the thin film and $\Delta\alpha = \alpha_f - \alpha_s$. The change in stress of the film was determined from the corresponding change in curvature. The absolute value of film stress requires the curvature, κ_0, of the unstressed film to be known. The absolute value was determined by measuring curvature at the temperature at which the film was sputtered. Because the reference curvature was taken at room temperature, the curvature and stress measurements were a "relative curvature" with respect to the curvature at room temperature.

Within the laser and optics cabinet, the MOS used a 659 nm fiber-coupled Peltier cooled laser diode package and temperature controller. The laser beam traveled through two separate etalons to create a two dimensional grid of parallel laser beams. The first etalon reflected a single laser beam through the etalon and split it into a one dimensional array of lower energy beams. The one dimensional array was reflected through a second etalon where the second array of beams resulted in a two dimensional grid.

The laser beam array was reflected off the film to a KP-M1A Hitachi 8-bit analog closed circuit detector (CCD) camera via optically flat mirrors. The camera was a high resolution, high-sensitivity, anti-blooming, monochrome CCD detector that was processed through the MOS computer. The camera's frame grabber provided less than ± 5 ns jitter at up to a 30 Hz frame rate. The mirrors automatically adjusted the beam as

thermal drift occurred during heating. Figure 4.9 shows the laser, camera, etalons, and mirrors.

The vacuum was provided with a Pfeiffer MVP 015-2 diaphragm vacuum pump, and a Pfeiffer TMH 071 P turbomolecular drag pump. Operating together, the pumps were designed to maintain a vacuum of 10^{-7} mbar. Nitrogen gas was introduced to the heating chamber with a mass flow controller capable of 200 cm^3/hr to regulate chamber pressure.

Figure 4.8:   MOS wafer bow measurement tool housing the laser and optics in the upper half and the heating chamber, power supply and controls in the lower half.
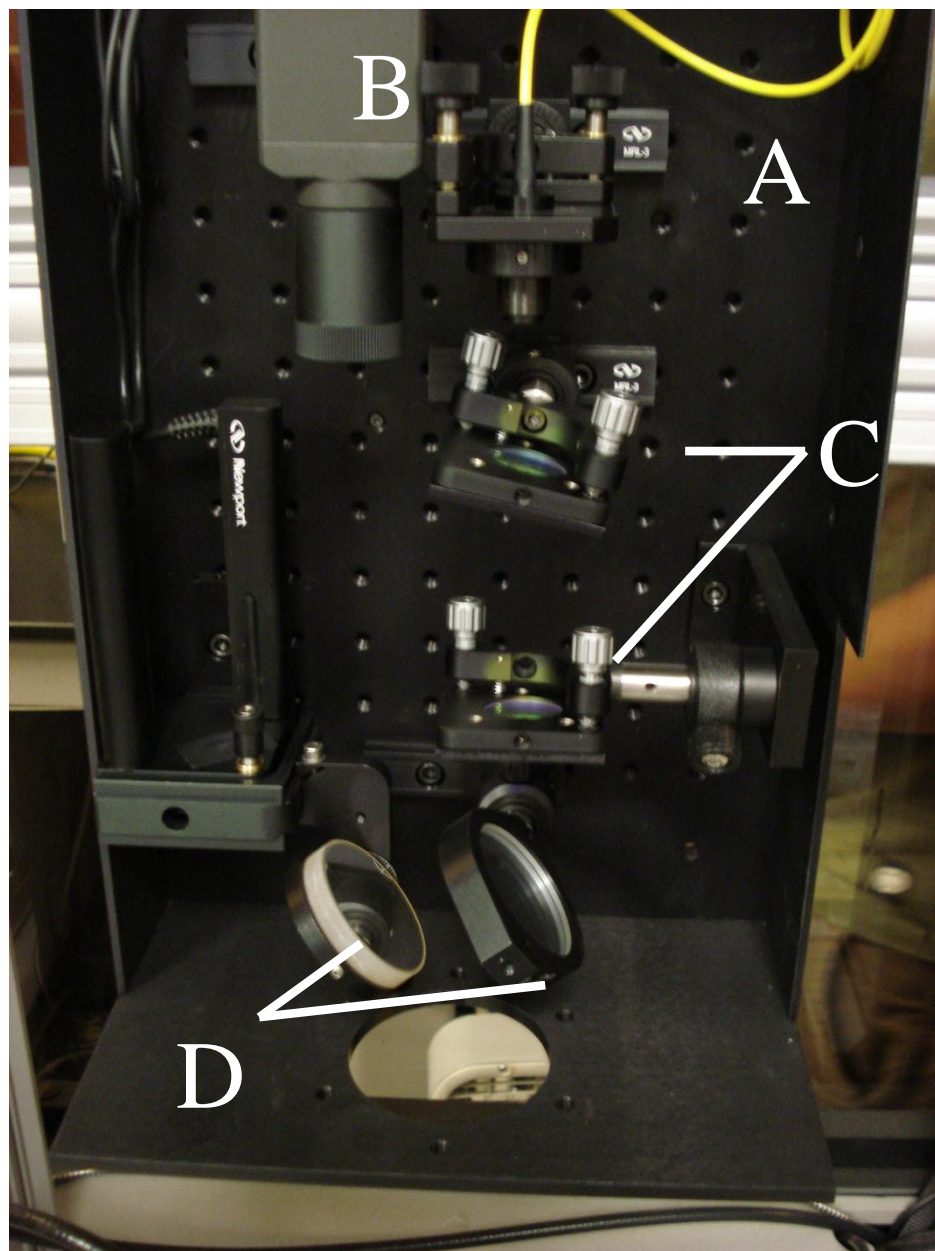
Figure 4.9: Internal view of the laser and optics cabinet containing A) laser, B) CCD camera, C) etalons, and D) mirrors

4.7 X-Ray Diffraction (XRD)

Texture measurements were performed by X-ray diffractometry in a θ-2θ

configuration, using a Bruker D8 Discover X-ray diffractometer (Figure 4.10) equipment

with Cu K$_\alpha$ radiation of wavelength λ = 1.54 angstroms (Å) and equipped with a Göbel

mirror. The sample was rotated about the out of plane film axis. The 2θ angle was

coupled and varied between 30° and 90°, where $\theta_1 + \theta_2 = 2\theta$. The distance from the

sample to the area detector was approximately 15 cm.
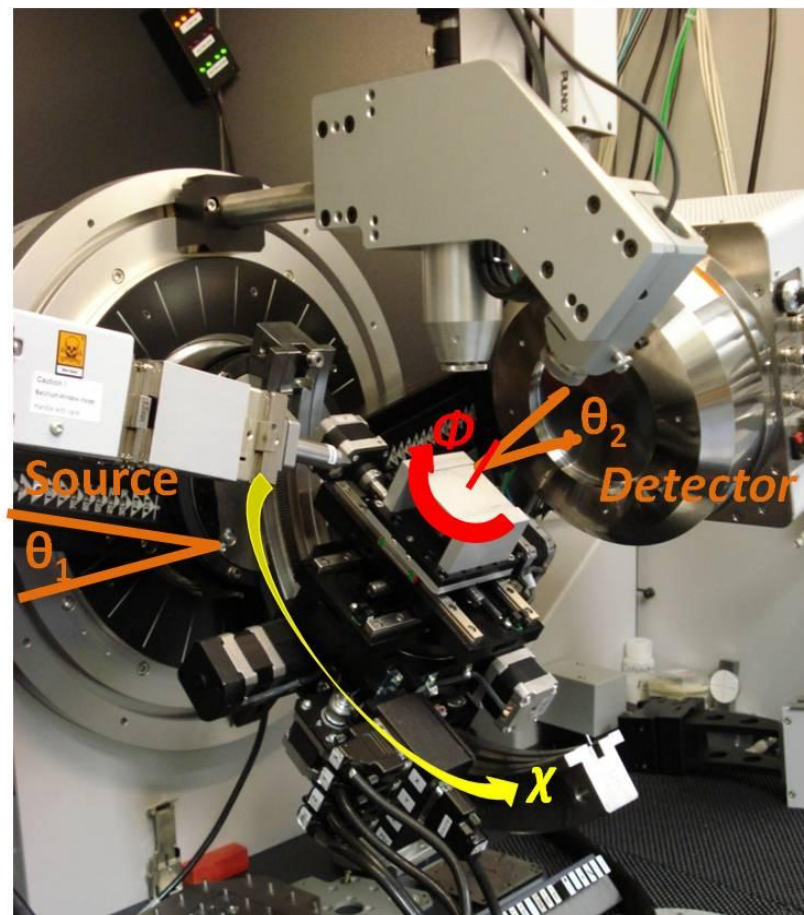
Figure 4.10: XRD with a parallel beam set up. Θ_1 is the x-ray source angle of inclination. Θ_2 is the detector angle of inclination. Φ (Phi) is the rotation about the normal plane of the sample. χ (Chi) is the rotation indicated (yellow).

4.8 Focused Ion Beam

Focused ion beam (FIB) technique uses a focused beam of ions to scan the surface

of a specimen or sputter away material. Application of a very high electric field onto a

liquid metal ion source (LMIS) generates ions, which are focused by an electrostatic lens.

Bombardment of the sample surface by extracted ions from the LMIS results in the

generation of secondary electrons, ions, and sputtered material. These different kinds of

generated species were used for various functions of the FIB, such as imaging due to secondary electrons generated and sputtering with the ion beam. FIB systems are mostly used in semiconductor industry and in 1993 there were approximately 150-200 commercial systems in operation worldwide [40]. The primary advantage of FIB was the capability to form an image of the specimen and then precisely mill the material away from selected areas.

The film thicknesses were measured using a Quanta 3D FEG Focused Ion Beam with EDS/EBSD operated with a Ga^+ ion source at 30 keV. The spatial resolution was 1.2 nm at 30 kV (secondary electrons), 2.5 nm at 30 kV (backscattered electrons), and 2.9 nm at 1 kV (secondary electrons). Each sample was cleaved to 5 mm x 5 mm, carbon taped to the stage, and held in a vacuum of 7×10^{-3} Pa. 200 nm of platinum was deposed on the surface to protect the film while in the ion beam. The stage was rotated 52° into the ion beam. Another platinum layer, 1 μm, was then deposited with the ion beam. The film was cross sectioned through the platinum layer with the ion beam set at 1.0 nA. A second pass at 0.1 nA was used to clean any debris or rough edges left during the cross-section process. The film thickness was then measured using the attached SEM calibrated to adjust for the 52° offset.

CHAPTER 5: RESULTS

It was shown in [16, 17] that Ni-Mn-Ga film compositions have similar saturation magnetization and phase transformation temperatures as their bulk Ni-Mn-Ga counterparts. It was also shown that in the form of films, FMSA's show a MFIS due to substrate-film adhesion. It was assumed that the composition and material property relationship for bulk discussed above was true for the sputtered films.

5.1 Sputtering

The results of the initial characterization of the sputter tool to obtain parameters for maximum thickness (Figure 5.1) show that film thickness increased as argon pressure was decreased. At 3 mTorr, the 50 and 75 Watt thickness doubled compared to 8 mTorr sputtering.

The composition map (Figure 5.2) indicates the range of compositions obtainable under constant chamber pressure, substrate temperature, and time. Power to each target was varied independently, while all previously mentioned parameters were held constant. The goal was to produce films with either a 10M or 14M structure. A composition of $Ni_{50}Mn_{28.6}Ga_{21.4}$ atomic percent was chosen as the target film composition. This composition in bulk Ni-Mn-Ga resulted in a 10M crystal structure with a martensite transformation temperature above 30 °C [34].
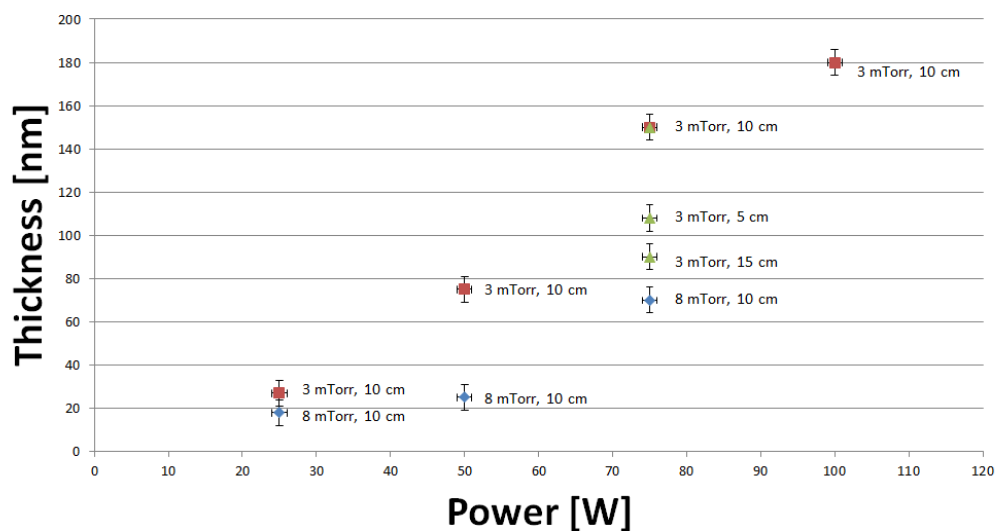
Figure 5.1: Plot showing pressure and power effects on film thickness. Three working distances, 5 cm, 10 cm, and 15 cm, and two pressures, 3 mTorr and 8 mTorr, were used to obtain a maximum sputter rate for Ni-Mn-Ga.
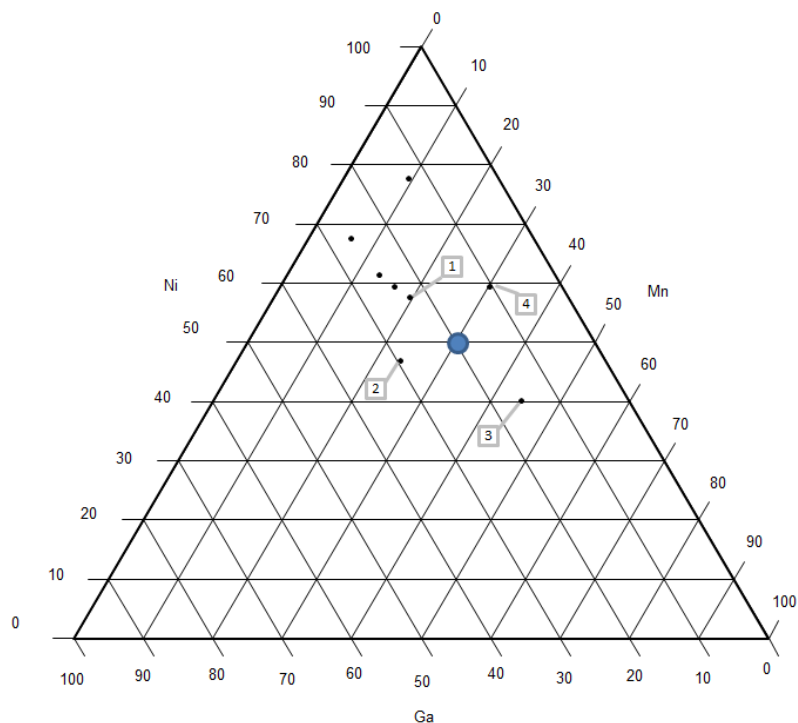
Figure 5.2: Ternary composition map showing the targeted composition at $Ni_{50}Mn_{30}Ga_{20}$ (large dot) and the compositions from the DOE that surrounded the targeted compositions (small dots).

Table 5.1 lists the sputter powers and respective compositions for the four films surrounding the targeted composition. Linear interpolations between the four points were used to iteratively approach the target composition.

Table 5.1:   Power and composition of the four DOE points surrounding the targeted composition area

Point	Target	Power [W]	Composition [at.%]
1	Ni	50	57.54
	Mn	50	19.65
	NiGa	50	22.82
2	Ni	15	46.93
	Mn	50	23.50
	NiGa	50	29.58
3	Ni	15	40.13
	Mn	50	44.35
	NiGa	15	15.51
4	Ni	50	59.41
	Mn	50	30.16
	NiGa	15	10.45

The nickel, manganese and nickel-gallium targets were each characterized to determine a sputter rate versus gun power. Five thicknesses at 0 W, 15W, 30 W, 50 W, and 70 W respectively and a linear fit through the points were used to determine the sputter rate of the nickel target. Only three manganese thicknesses could be measured (at 30 W, 40 W, and 50 W). A linear fit through the three points and zero thickness at 0 W was used to find the manganese target sputter rate. The nickel-gallium sputter rate was determined from 6 points. The Ni-Ga plot is shown in Figure 5.3. The error bars were determined by the standard deviation of the film thickness measurements from SEM images captures after the FIB cross sectioning. Table 5.2 summarizes the sputter rates for each target source.
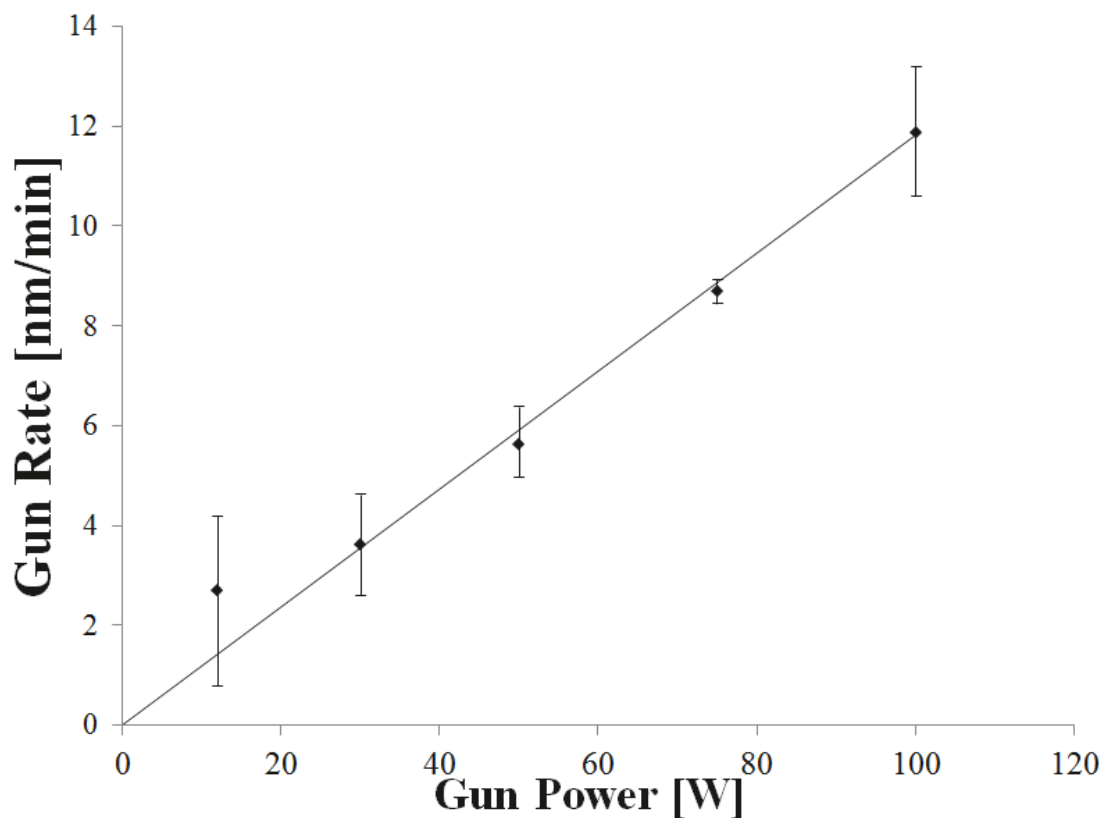
Figure 5.3: Rate versus power plot for the nickel-gallium target.

Table 5.2: Sputter rate for each target at 3 mTorr and a 10 cm working distance.

Gun	Rate [nm/min W]
Ni	0.07 ± 0.01
Mn	0.08 ± 0.01
Ni-Ga	0.12 ± 0.02

Figure 5.4 shows a range of bulk Ni-Mn-Ga compositions, where the phase is known for each sample [33, 34]. This composition plot was used to assign predicted phase regions on the ternary phase diagram in Figure 5.5. For overlapping regions, multiple phases have been reported [32, 33]. The four large squares in Figure 5.5 are the

film compositions from the DOE that surrounded the targeted composition. The numbers (#/#/#) represent the gun powers of each gun, Ni, Mn, and Ni-Ga respectively.

The ternary phase diagram (Figure 5.6) contains the films sputtered and the location relative to the phase regions determined in Figure 5.4. Table 5.3 lists the films sputtered for this study. The size of the marker box indicated the compositional error.
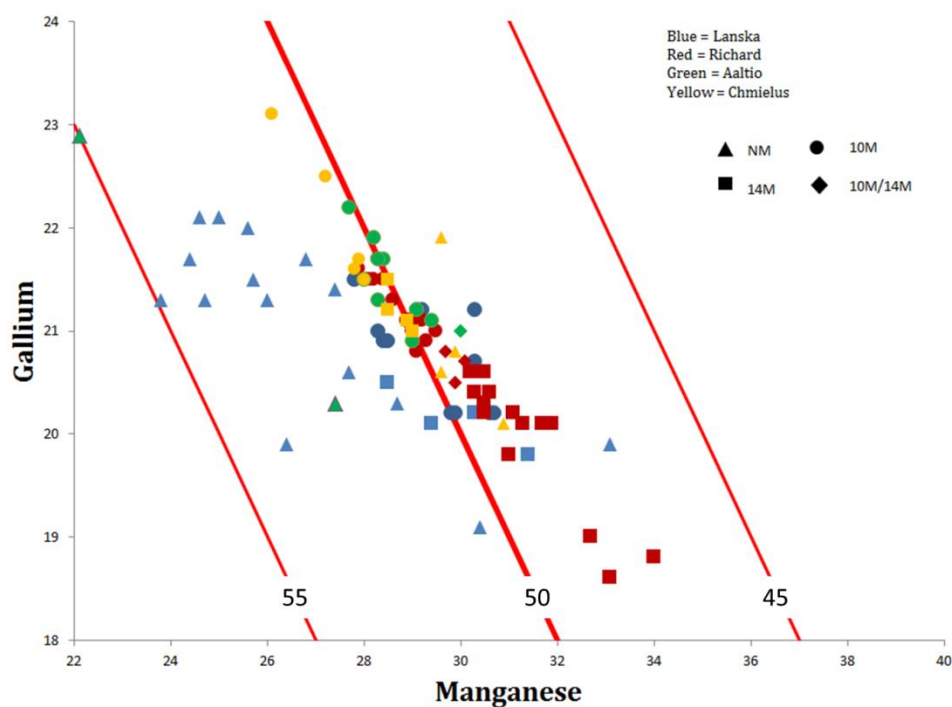
Figure 5.4: **Phase diagram of Ni-Mn-Ga phases as reported by [32, 33]. Solid red lines indicate constant nickel content.**
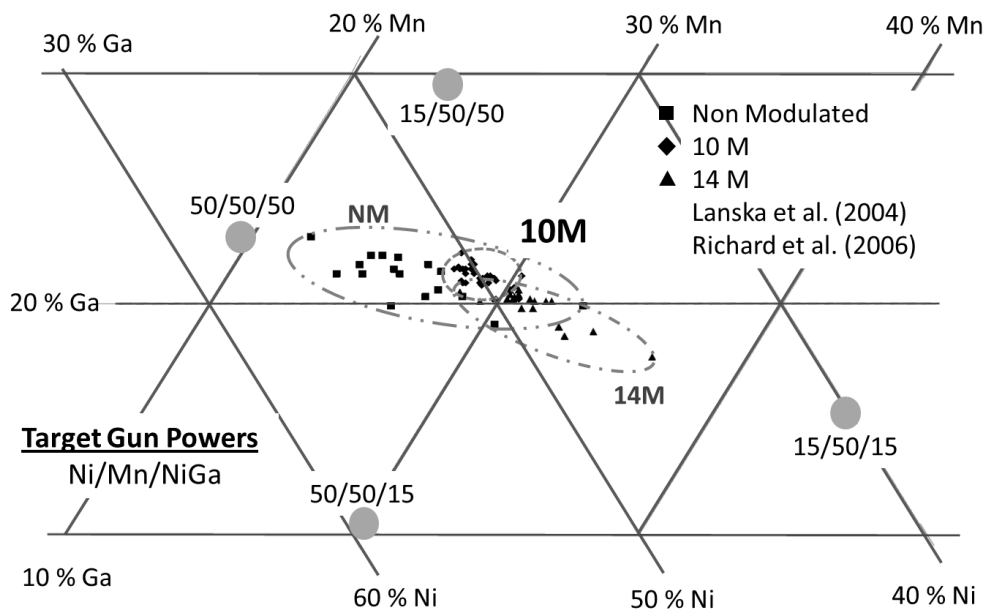
Figure 5.5: Ternary phase diagram showing the expected phase regions for 10M, 14M, and NM at room temperature, as reported by [32, 33]. DOE film compositions are indicated as grey dots. Reported martensite phases are represented as 10M diamonds, 14M triangles, and NM squares [33, 34].
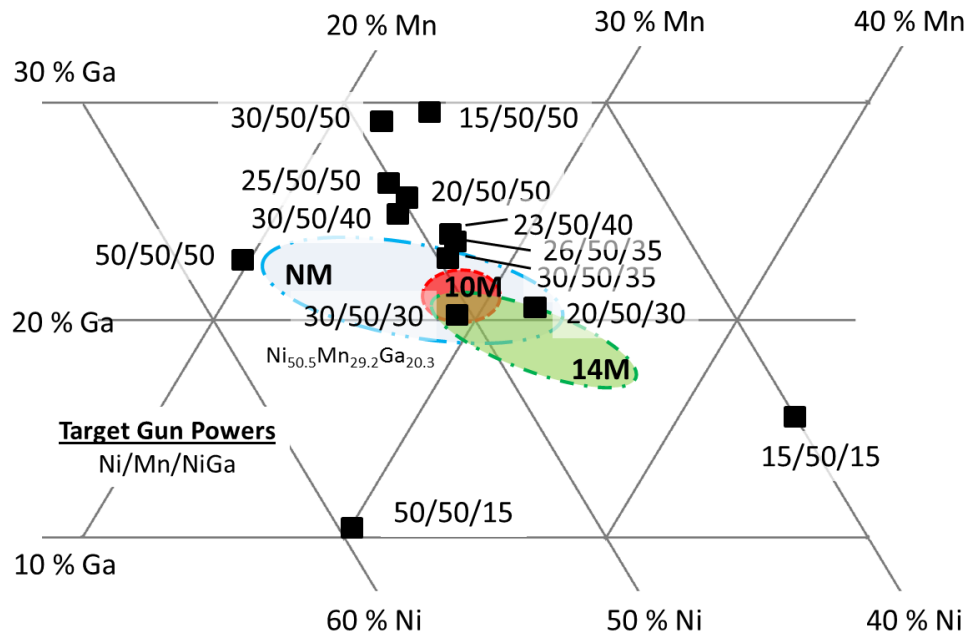
Figure 5.6: Ternary phase diagram showing the expected phase regions for 10M, 14M, and NM at room temperature as determined from bulk literature data [32, 33]. Sputtered film compositions are indicated by the gun powers used and represented as black squares.

Table 5.3: This table shows the gun power, composition, and thickness of films used in this study. Note P$_i$ is power with units of watts where i is the element or elements sputtered.

| Film	P$_{Ni}$	P$_{Mn}$	P$_{NiGa}$	Time [min]	Thickness [nm]	Composition [at. %]		
						Ni	Mn	Ga
1	15	0	0	60	52	100	0	0
2	30	0	0	60	134	100	0	0
3	50	0	0	60	172	100	0	0
4	100	0	0	60	215	100	0	0
5	0	0	12	60	163	49.38	0	50.63
6	0	0	30	60	218	52.27	0	47.74
7	0	0	50	60	338	51.53	0	48.47
8	0	0	75	60	522	52.76	0	47.25
9	0	0	100	60	714	53.79	0	46.21
10	0	15	0	60	-	0	100	0
11	0	20	0	60	-	0	100	0
12	0	30	0	60	135	0	100	0
13	0	40	0	60	196	0	100	0
14	0	50	0	60	240	0	100	0
15	50	50	50	60	796	57.54	19.65	22.82
16	50	50	15	60	472	59.41	30.16	10.45
17	15	50	15	60	-	40.13	44.35	15.51
18	15	50	50	60	598	46.93	23.50	29.58
19	15	15	15	60	213	61.36	13.23	25.42
20	20	50	50	60	606	49.74	24.58	25.68
21	25	50	50	60	669	50.13	23.60	26.27
22	20	50	30	60	508	47.50	32.02	20.49
23	30	50	30	60	508	50.50	29.20	20.30
24	30	50	35	60	515	49.52	27.61	22.87
25	23	50	40	60	627	48.83	27.23	23.94
26	26	50	35	60	502	48.93	27.36	23.71
27	30	50	40	60	628	50.48	24.53	25.00
28	30	50	50	60	749	48.90	21.83	29.28
29	100	30	30	60	735	77.58	9.39	13.03
30	30	30	30	60	491	59.46	16.49	24.06
31	100	30	100	60	1203	67.56	6.14	26.31

5.2 Vibrating Sample Magnetometer

The saturation magnetizations, which were similar to the 45-60 emu/g value seen for bulk Ni-Mn-Ga, of six films of varying composition showed ferromagnetism after sputtering without post-process annealing [5, 41] (Figure 5.7). The negative linear slopes after saturation were due to the diamagnetic behavior of the silicon substrate. The slopes differed relative to the thickness of the film. The diamagnetic effects were reduced as film thickness increased. Figure 5.8 shows the hysteresis of the sputtered film from target gun powers 30, 50, 30 for Ni, Mn, and NiGa, respectively.
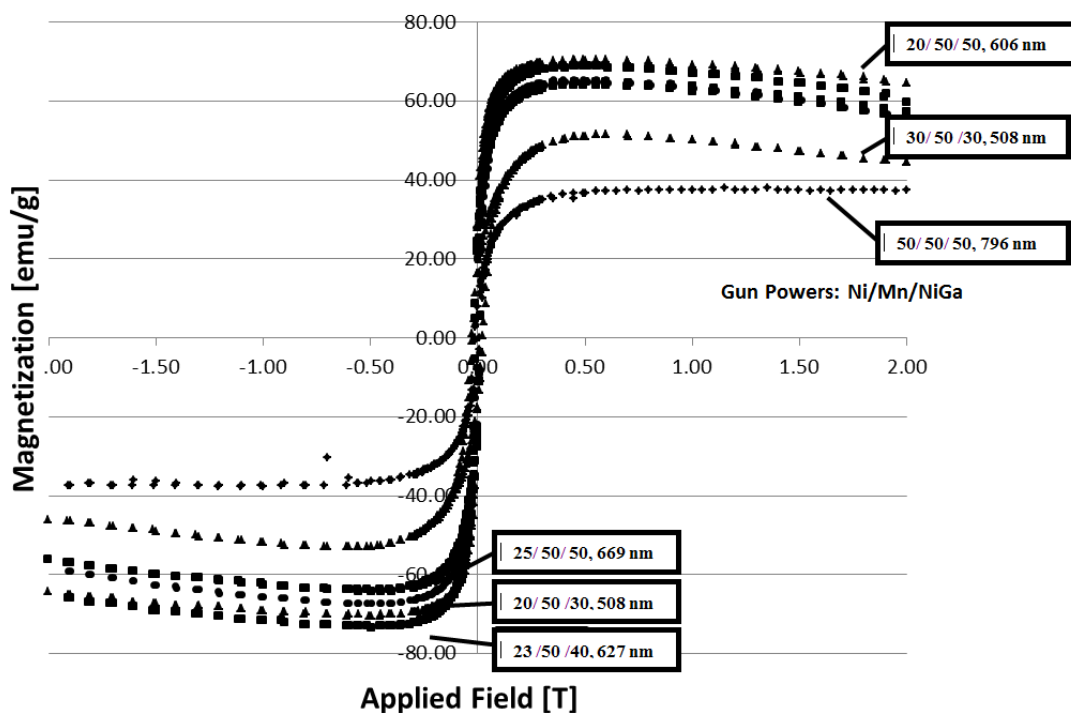
Figure 5.7: **Magnetization hysteresis of as sputtered films. Target gun powers of each film are for Ni, Mn, and NiGa, respectively. The sputter time was 60 minutes onto a 500 °C heated substrate at a constant argon pressure of 3 mTorr**
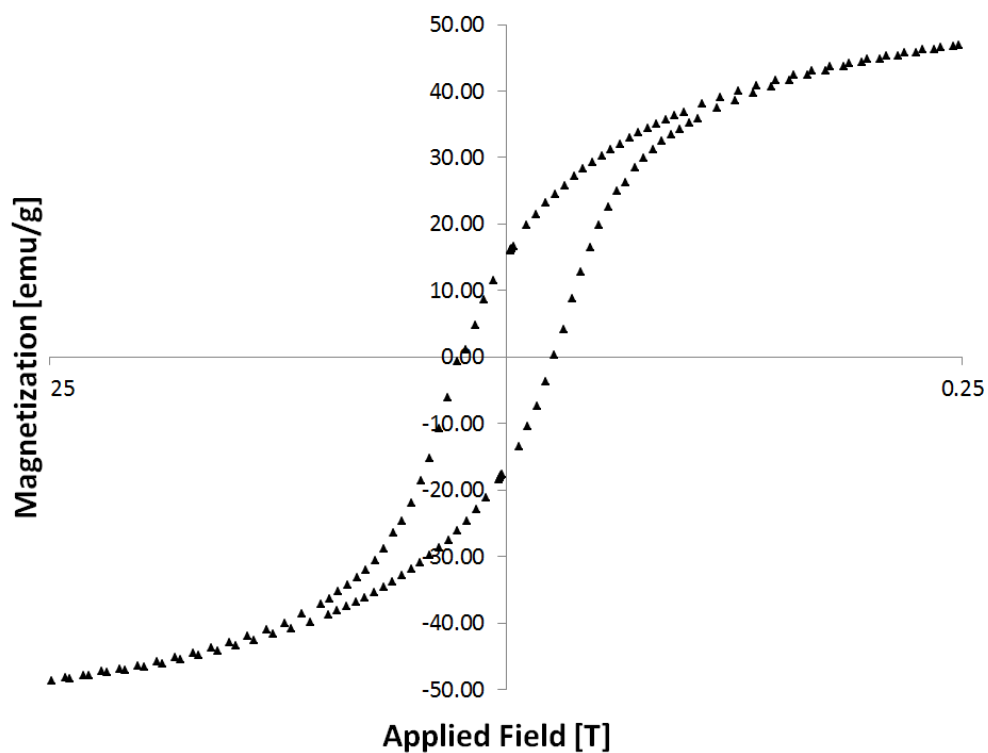
Figure 5.8: **Magnetization hysteresis of as sputtered film from target gun powers 30, 50, 30 for Ni, Mn, and NiGa, respectively.**

In the magnetization vs. temperature curve (Figure 5.9) for the as-deposited film, composition $Ni_{50.5}Mn_{29.2}Ga_{20.3}$, the Curie temperature was determined to be 90 °C $\pm$ 1 °C. No martensitic transformation is seen, which will be addressed in Section 5.3.
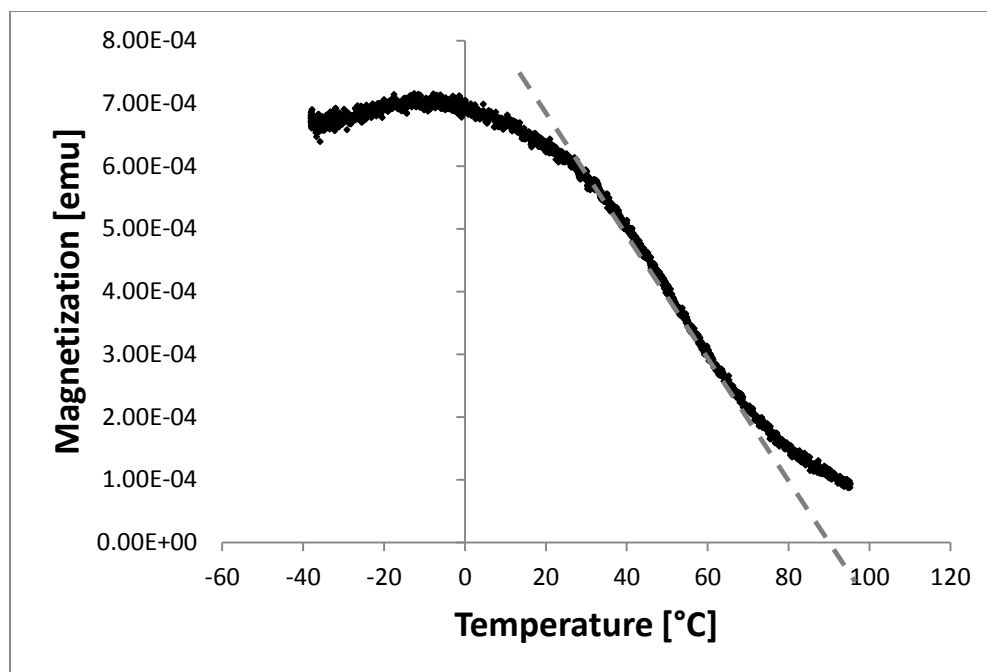
Figure 5.9: **Magnetization vs. temperature curve for an as sputtered film. The film has composition: Ni$_{50.5}$Mn$_{29.2}$Ga$_{20.3}$. The target powers were: Ni: 30 W, Mn: 50 W, and NiGa: 30 W. The final film thickness was 500 nm on a 500 μm silicon substrate.**

5.3 Wafer Curvature Deflectometery

A change in film stress with temperature can reveal crystallographic transformation temperatures in FSMA thin films. MOS Wafer Curvature Deflectometry was used to examine transformation temperatures in the sputter deposited Ni$_x$Mn$_y$Ga$_{x-y}$ thin films. Figure 5.10 is a plot of film stress vs. temperature for the Ni$_{50.5}$Mn$_{29.2}$Ga$_{20.3}$ film. The martensite transformation temperatures were defined as the point of intersection of the tangent lines as shown in Figure 5.10. The hysteresis was due to the martensitic phase transformation. The linear region (T > 150 °C) indicated normal thermal elastic behavior.
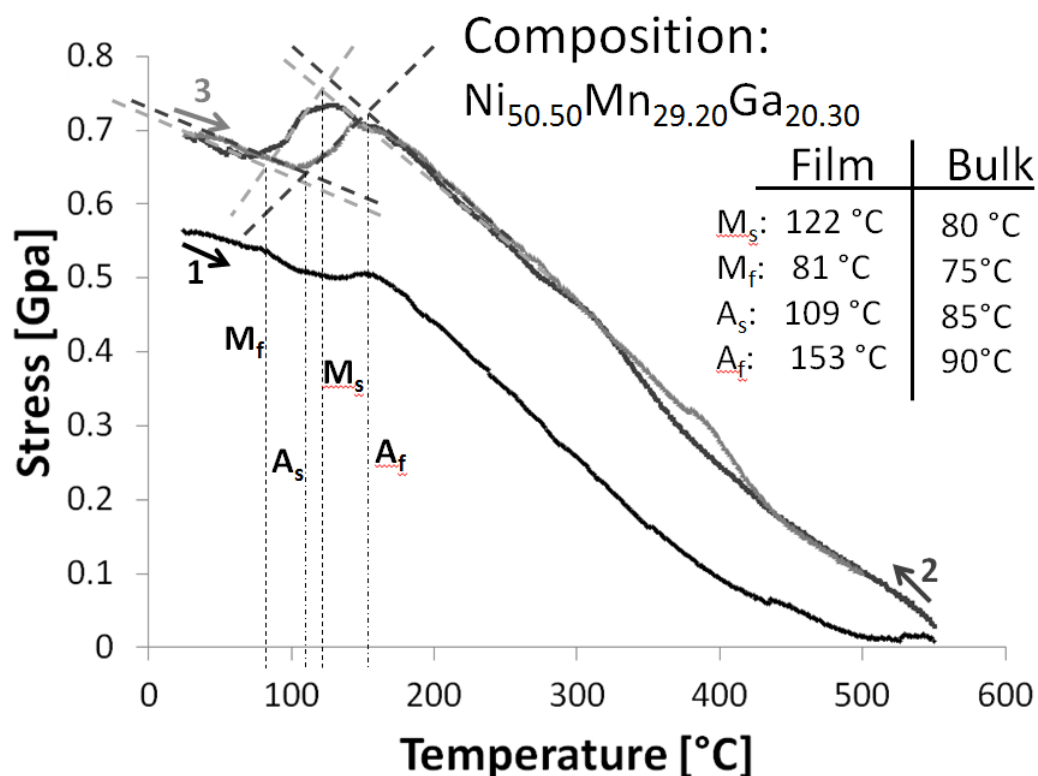
Figure 5.10: Stress vs. temperature curve for an as sputtered film. The film has composition: Ni₅₀.₅Mn₂₉.₂Ga₂₀.₃. The film was ramped to 550 °C and back to room temperature at 10 °C/min and repeated for 500 °C. The hysteretic anomaly is from the martensitic phase transformation. The linear region (*T* > 150 °C) indicates a normal thermal elastic behavior. M = martensitic; A = austenitic; s = start; f = finish.

5.4 X-Ray Diffraction

The XRD spectrum of the as-deposited film (Figure 5.11) shows the strong silicon substrate reflection at 69° and three peaks ~3° apart around 80°. Also in Figure 5.11, a single 2θ scan centered on 44°, which was rotated to 33° in Chi. The scan showed two broad reflections with peak positions at 42.9° and 44.3°. The peak on the right contained a shoulder indicating a third reflection at 45°. The broad peaks were indicative of the amorphous and polycrystalline nature of the sputtered films. The peak locations were determined from a Lorentzian fit of the spectrum (Figures 5.12, 5.13). Three reflections

around 44° and three reflections around 80° were typical of bulk Ni-Mn-Ga with a
Psuedo-Orthorhombic 14M structure peak simulation (Figure 5.14). The peak simulations
for Ni-Mn-Ga austenite, 10M, 14M, and NM can be seen in appendix. The calculated
lattice parameters were 0.618 nm, 0.577 nm, and 0.549 nm for a, b, and c, respectively,
and agree well with those obtained by Sozinov et al. [42].

XRD texture measurements reveal a strong 211(fiber, when grown on a heated
substrate, Ni-Mn-Ga films develop a strong 110 fiber texture [19]) texture. The 14M
simulation (Figure 5.14) suggests that the predominant peaks are of the 220 type.
However, in Figure 5.11, at 0° chi, the strongest peaks were of the 422 type. When the
film was rotated to 33° chi, the 220 type peaks reach a maximum. Therefore, it appears
that the film had a 211 fiber texture.
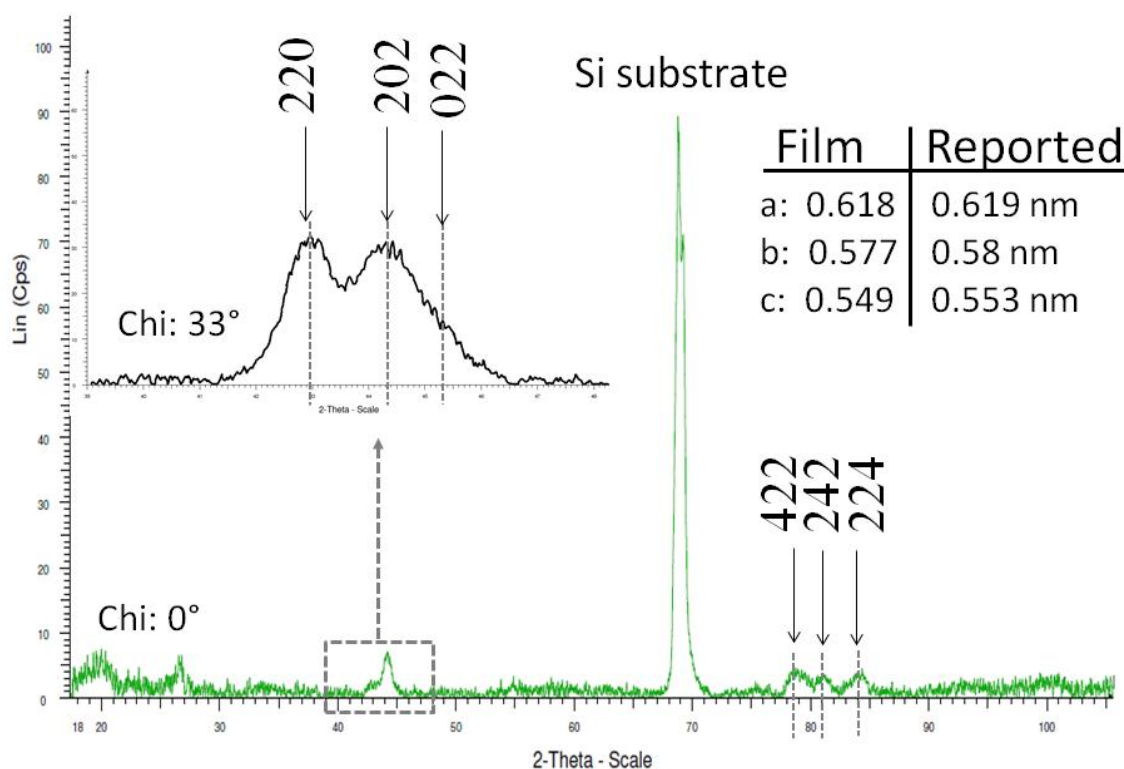
Figure 5.11:   XRD of as sputtered Ni50.5Mn29.2Ga20.3 film on silicon substrate.
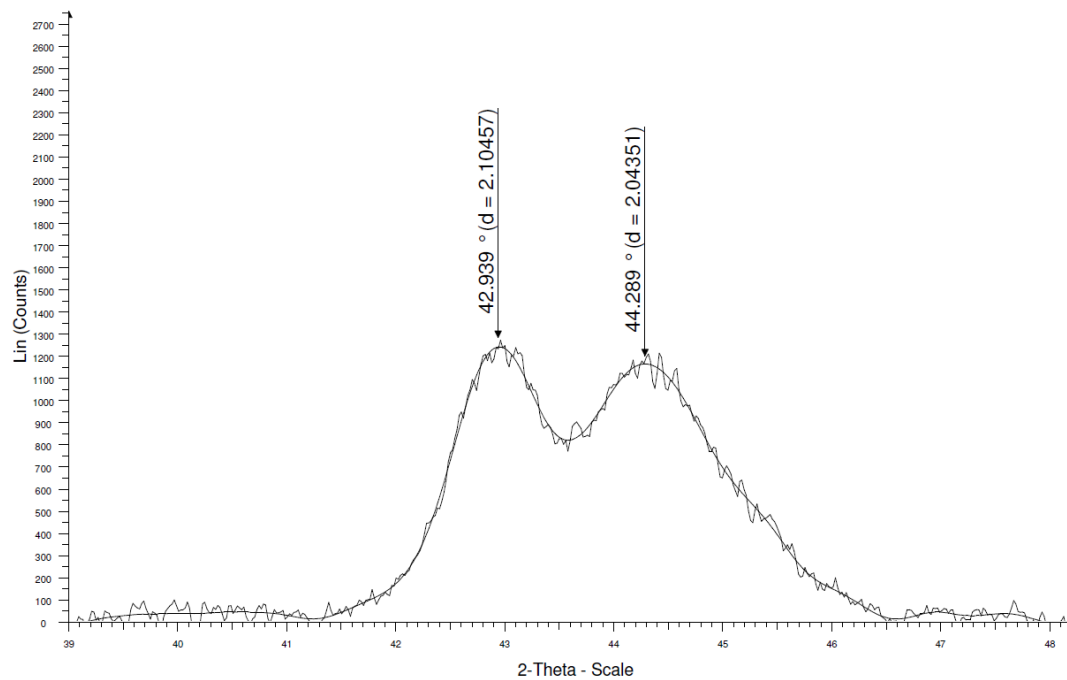
Figure 5.12: Lorentzian fit of 220 type reflections of as sputtered Ni$_{50.5}$Mn$_{29.2}$Ga$_{20.3}$ film on silicon substrate.
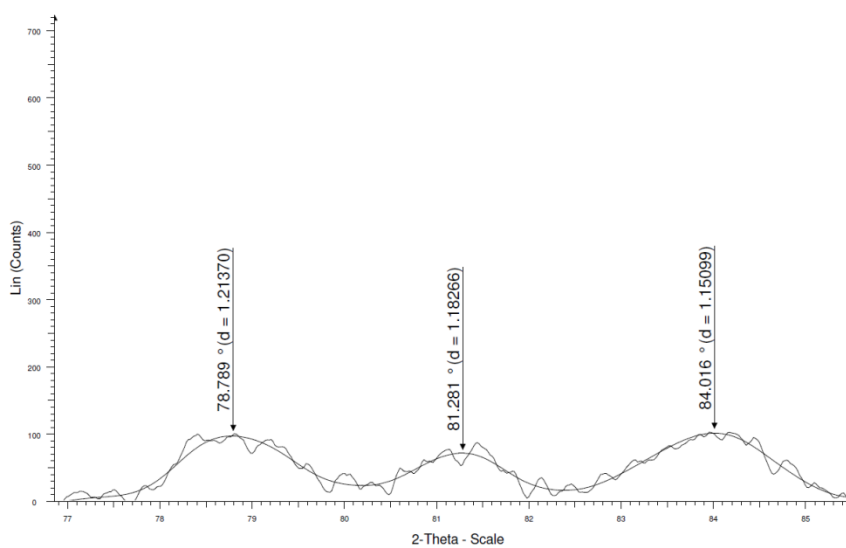
Figure 5.13: Lorentzian fit of 422 type reflections of as sputtered Ni$_{50.5}$Mn$_{29.2}$Ga$_{20.3}$ film on silicon substrate.
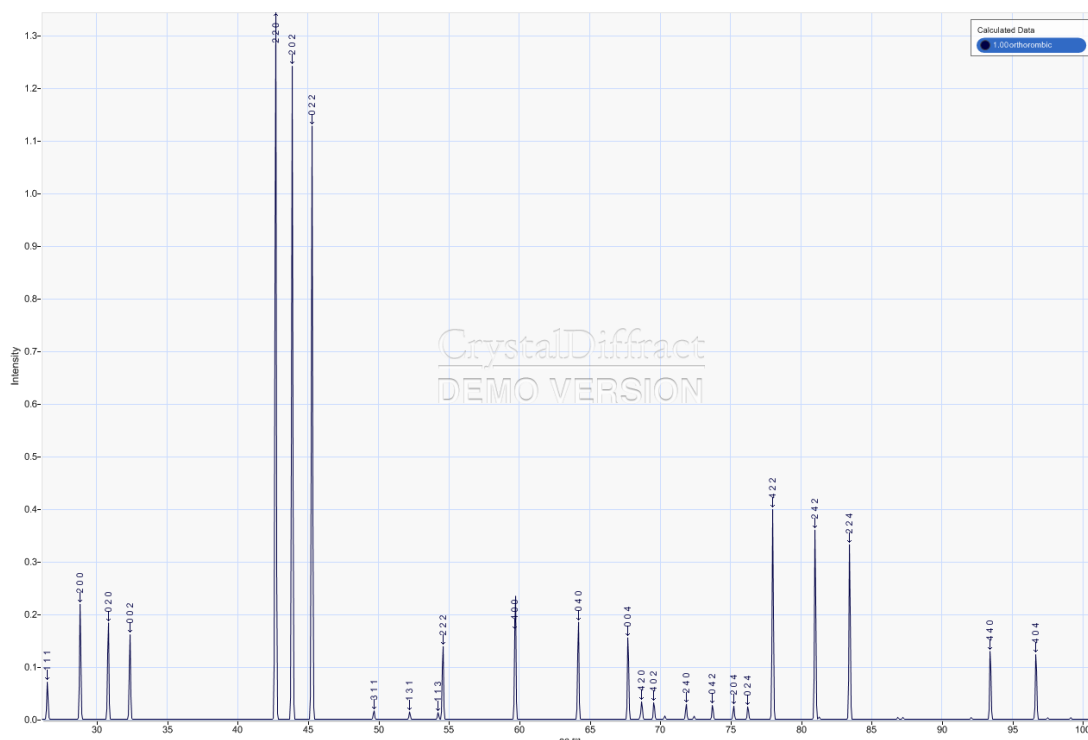
Figure 5.14:   Reflection peak simulation of Ni-Mn-Ga 14M structure.

5.5 TEM

The microstructure of the $Ni_{50.5}Mn_{29.2}Ga_{20}$ film was characterized with a JEOL 2100 LaB_6 transmission electron microscope (TEM). The TEM revealed equiaxed grains with an average grain size of 100 nm and a 14M martensite structure (Figure 5.15). Unlike films deposited over single crystal substrates, in this case the film resided on the native oxide layer of the substrate, which hindered the epitaxial growth and promoted the formation of a small grained polycrystalline film.
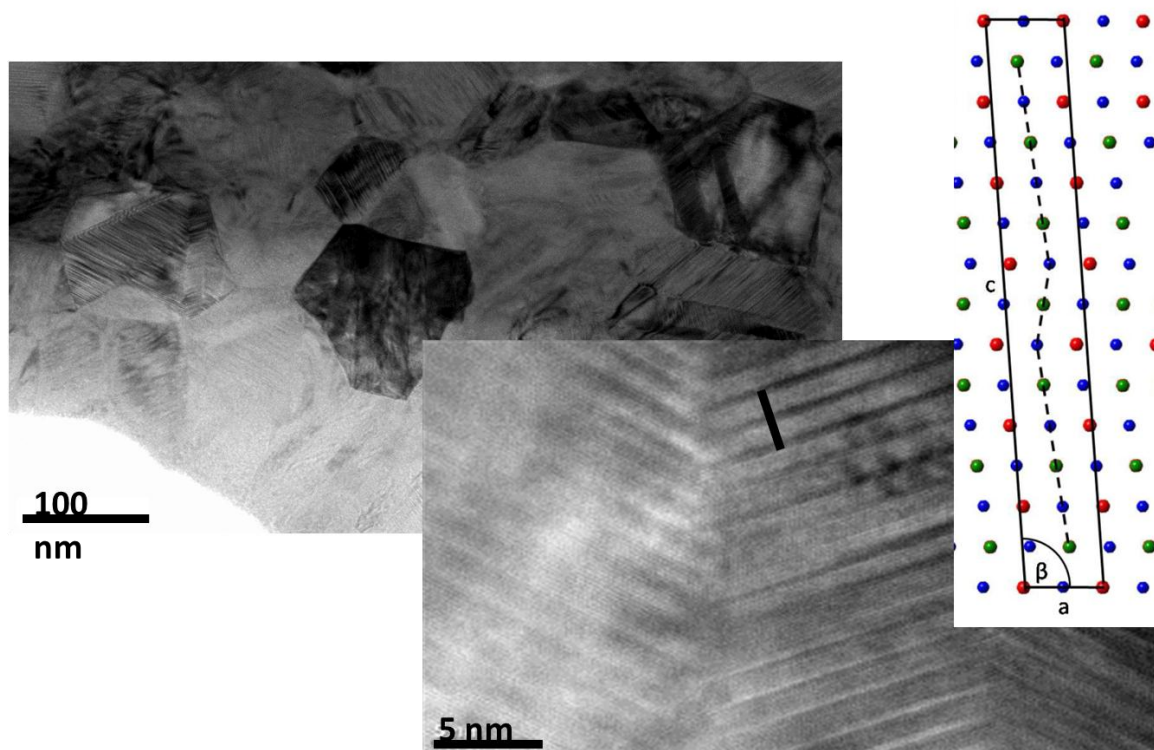
Figure 5.11: TEM image of Ni$_{50.5}$Mn$_{29.2}$Ga$_{20.3}$ film on silicon substrate showing grain size and modulation.

CHAPTER 6: DISCUSSION

The objective of the study was to sputter deposit a Ni-Mn-Ga 10M and 14M thin film at 500 °C by varying the power of three sputter source targets simultaneously to control film composition. It has been shown that ferromagnetic microstructured films were produced using "tri"-target sputtering without post annealing. The following sections discuss the evidence of achieving this goal.

6.1 General Discussion

Substrate curvature measurements, VSM, XRD, and TEM measurements were all performed to investigate the mechanical, structural, and magnetic properties of Ni-Mn-Ga MSMA alloy thin films deposited on silicon substrates. The wafer curvature deflectometry measurements revealed information about the film stress, as well as the martensitic and austenitic phase transformation temperatures of the films. VSM measurements revealed the Curie temperatures and saturation magnetization of the films. X-ray diffraction measurements measured the crystallographic texture of the films. TEM measurements display structure and grain size of the films

The films used to investigate mechanical, structural, and magnetic properties were "tri"-sputtered with gun powers of Ni: 30 W, Mn: 50 W, and NiGa: 30 W, at a growth temperature of 500 °C and yielded films of $Ni_{50.5}Mn_{29.2}Ga_{20.3} \pm 0.5$ atomic percent, verified via EDS. The Ni-Ga films show an increase in nickel and a decrease in gallium

as target power was increased (films 5-9, Table 5.3). There was a shift upward in gallium content at 50 W, but then the trend continues.

6.2 Magnetic Properties

Curie temperature and saturation magnetization measurements reveal that the stress state of the film do not have a significant effect on these parameters of the sputtered films as they are in agreement with the reported values for bulk alloys with the same composition.

6.3 Mechanical Properties

To better understand the curvature results, an illustration of the stress evolution as a function of temperature in Ni-Mn-Ga films during and after their deposition is shown in Figure 6.1. Each film was sputtered at 500 °C for 60 minutes. At 500 °C, the film is in a fully relaxed state. Upon cooling, in the high temperature region, diffusion relaxes film stress, which develops because of the thermo-elastic mismatch (Equation 8). At lower temperatures, diffusion decreases and the film begins to develop an in plane tensile stress. In accordance with Equation 8, this stress evolution is linear in temperature. As the film cools below the martensite transformation temperature, the phase transformation allows the film to relax [43]. Once the film has cooled to room temperature, some residual stress, $\sigma_{residual}$, remains. Upon heating, a phase transformation continues until the martensite finish temperature is reached. As the temperature increases, diffusion occurs, until the film reaches a fully relaxed state at the deposition temperature.
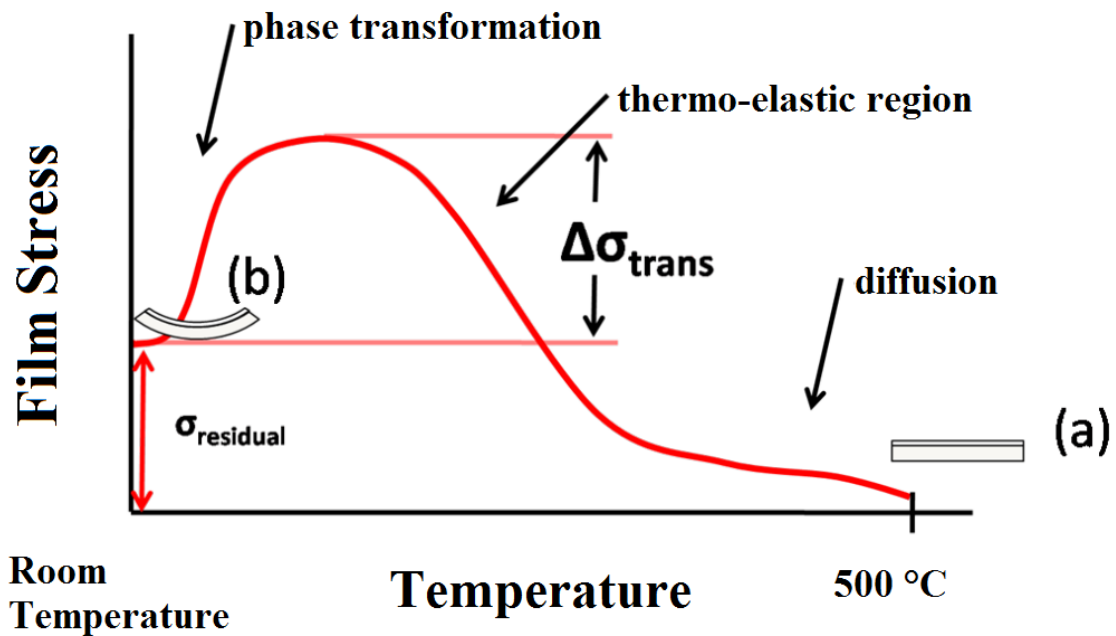
Figure 6.1: Schematic of the stress evolution in Ni-Mn-Ga thin films during heat treatment. At the annealing temperature, the film is in a fully relaxed state, with zero curvature (a). As the film cools, diffusion inhibits film stress. In the thermal elastic region, stress behaves in accordance with Equation 3. The martensitic phase transformation is exhibited by a stress relaxation. The residual stress, $\sigma_{residual}$, present at room temperature induces a curvature in the substrate (b).

The calculated lattice parameters decrease by 1% from the reported values [42]. Considering typical values of E_a=40 GPa and E_m=20 GPa from mechanical measurements on polycrystalline fine-grained Ni-Mn-Ga alloys [19], a Poisson ratio of 0.3 and the residual stress seen in Figure 5.10, $\sigma_{residual} = 700 \pm 25$, the calculated relative unit cell volume change between the martensite at 30 °C and austenite at 170 °C would be a decrease of approximately 1%, agreeing with the calculated lattice parameter results from XRD.

6.4 Microstructure

XRD texture measurements of the $Ni_{50.5}Mn_{29.2}Ga_{20.3}$ film appear to show a 211 texture, which is different from the strong (022) texture reported by Chernenko et al. [19] for films deposited with elevated substrate temperatures. The peaks observed in the XRD measurement correspond to the pseudo-orthorhombic 14M-martensite. This 14M matensite can also be seen in the TEM (Figure 5.15). Although the composition suggest a 10M martensite, [44] suggests that a shift from 10M to 14M to 2M (NM) will result as film stress is increased.

Pure metal films show grain growth at temperatures as low as 20 percent of the melting temperature [45]. Grain growth stops when the grain size is approximately twice the film thickness. This limit is controlled by the formation of grooves [46]. Grain growth and groove development are competing processes [47]. During normal grain growth, the driving force for growth is the reduction in total grain boundary energy. Grain sizes smaller than the film thickness will undergo normal grain growth until all grain boundaries intersect the top and bottom of the film. Once the grains in a thin film have formed columnar structures, normal grain growth ceases. Any subsequent growth occurs via abnormal grain growth where only a few grains continue to grow at the expense of the other grains.

Thin films deposited using sputter deposition have nanograins, which act as barriers for the propagation of dislocations, and hence the nanograins lead to strengthening of the material [48]. Larger grain sizes in thin films are shown to ease magnetic and shape memory effect due to reduced constraints from grain boundaries, easing re-orientation and phase transformation in grains [49].

6.5 Martensitic Transformation and Martensite Structure

It is known that for bulk Ni-Mn-Ga uniaxial compressive stresses shift the martensitic transformation temperature to higher temperatures than for a stress-free state [50, 51]. The shift of the martensite transformation temperature can be described by the Clausius-Clapeyron type equation [51]:

$$\frac{d\sigma_c}{dT} = -\frac{\Delta S}{\varepsilon V_m} = -\frac{\Delta H}{T_0 \varepsilon V_m} \tag{9}$$

where ΔS and ΔH stand for the entropy and enthalpy differences between the austenite and martensitic phases respectively, T_0 is the equilibrium temperature, ε is the transformation strain, and V_m the molar volume. For low stress samples, 100-200 MPa [51], the martensite transformations were 28-52 °C [33]. The $Ni_{50.5}Mn_{29.2}Ga_{20.3}$ film studied here would have a martensitic transformation near 117 °C according to [51], due to the 700 MPa stress in the film. The higher transformation temperature in the film appears reasonable due to the stress state of the film. It is seen in the data provided by Richard et al. [34] that the 14M structure has a higher transformation temperature than the 10M. Based on film structure and stress in the film, a ~70 °C shift is seen in the martensitic transformation temperature.

6.6 Conclusion

The research presented in this thesis was performed to characterize the properties of Ni-Mn-Ga alloys processed via "tri'-deposition sputter methods by controlling film composition by adjusting only the power to each target. In this thesis, we were able to produce thin films of various targeted compositions, specifically one of $Ni_{50.5}Mn_{29.2}Ga_{20.3}$ with a martensite transformation of 122 °C, saturation magnetization of 50 emu/g, and

Curie temperature of 90 °C. The film exhibited a reversible phase transformation, which was shifted to a higher temperature due to the film stress. A 10M structure was targeted via composition selection. A 14M structure was revealed from XRD and TEM experiments. The 14M structure may be stabilized by film stress.

CHAPTER 7: OUTLOOK

To develop Ni-Mn-Ga thin films that can be used as future MEMS actuator materials, lower residual film stress, larger grain size, and accurate control of martensite phase would be desirable.

The texture of the Ni-Mn-Ga alloys may have an influence on the properties examined in this thesis. An in-depth analysis of the deviation of the (400) reflections perpendicular to the film surface via a pole figure should be measured to completely describe the film texture. Grain growth experiments, such as post annealing films near half the melting temperature, could also be completed to see the effects on texture and residual film stress. Because the sputter parameters were held constant for maximum sputter rates, a DOE on sputter pressure, working distance, and substrate temperature, could lead to better control of composition and microstructure at the specific target powers of Ni: 30 W, Mn: 50 W, Ni-Ga: 30 W.

An investigation of the Ni-Ga target could also be completed. The composition could be tracked over time and usage as well as a composition vs. target power DOE.

REFERENCES

[1]   F. Heusler, *uber magnetische Manganlegrierungen*, 1903.

[2]   J. W. Buehler, *WOL Oral History Supplement, NITINOL Re-Examination*, in
        <http://www.wolaa.org/files/Nitinol_Oral_History.pdf>. vol. **8**: WOLAA LEAF,
        2006.

[3]   K. Otsuka, C.M. Wayman (editors), *Shape Memory Materials*, Cambridge
        University Press, Cambridge, United Kingdom, 1998.

[4]   P. Müllner, V. A. Chernenko, M. Wollgarten, and G. Kostorz, *Large cyclic
        deformation of a Ni-Mn-Ga shape memory alloy induced by magnetic field*, J.
        Appl. Phys., vol. **92**, 2002.

[5]   K. Ullakko, J. K. Huang, C. Kantner, R. C. Ohandley, and V. V. Kokorin, *Large
        magnetic-field-induced strains in Ni2MnGa single crystals*, Applied Physics
        Letters, vol. **69**, pp. 1966-1968, 1996.

[6]   S. J. Murray, M. Marioni, S. M. Allen, R. C. O'Handley, and T. A. Lograsso, *6%
        magnetic-field-induced strain by twin-boundary motion in ferromagnetic Ni--Mn-
        -Ga*, *Applied Physics Letters,* vol. **77**, pp. 886-888, 2000.

[7]   P. Müllner, V. A. Chernenko, and G. Kostorz, *Large cyclic magnetic-field-
        induced deformation in orthorhombic (14M) Ni--Mn--Ga martensite*, Journal of
        Applied Physics, vol. **95**, pp. 1531-1536, 2004.

[8]   A. Sozinov, A. A. Likhachev, N. Lanska, and K. Ullakko, *Giant magnetic-field-
        induced strain in NiMnGa seven-layered martensitic phase*, Applied Physics
        Letters, vol. **80**, pp. 1746-1748, 2002.

[9]   C. Liu, Z.Y. Gao, X. An, H.B. Wang, L.X. Gao, W. Cai, *Surface characteristics
        and nanoindentation study of Ni–Mn–Ga ferromagnetic shape memory sputtered
        thin films*, Appl. Surf. Sci. **254**, pp. 2861-2865, 2008

[10]   V. A. Chernenko, M. Kohl, V. A. L'vov, V. M. Kniazkyi, M. Ohtsuka, O. Kraft,
        *Martensitic Transformation and Microstructure of Sputter-Deposited Ni–Mn–Ga
        Films*, Mater. Trans., **47**, 619624, 2006.

[11]   F. J. Castano, B. Nelson-Cheeseman, R. C. O'Handley, C. A. Ross, C. Redondo,
        F. Castano, *Structure and thermomagnetic properties of polycrystalline Ni–Mn–
        Ga thin films*, J. Appl. Phys., **93**, pp. 8492-8494, 2003

[12] V. A. Chernenko, M. Ohtsuka, M. Kohl, V. V. Khovailo, T. Takagi, Smart Mater. Struct., *Transformation behavior of Ni–Mn–Ga thin films*, Smart Mater. Struct., **14,** pp. S245-S252, 2005.

[13] P. Pörsch, M. Kallmayer, T. Eichhorn, G. Jakob, H. J. Elmers, C. A. Jenkins, C. Felser, R. Ramesh, M. Huth*, Suppression of martensitic phase transition at the Ni2MnGa film surface*, Appl. Phys. Lett., **93**, pp. 022501, 2008.

[14] E. Arzt , *Size effects in materials due to microstructural and dimensional constraints: a comparative review*, Acta Mater., **46**, 5611-5626, 1998.

[15] G. Kostorz , P. Müllner, *Magnetoplasticity*, Z. f. Metallkunde, **96**, 703-709, 2005.

[16] V. A. Chernenko, *Concepts and Physical Phenomena in Magnetic Shape Memory Science*, Adv. Mater. Res., **52**, 3-14, 2008.

[17] O. Söderberg , I. Aaltio , Y. Ge , O. Heczko , S. P. Hannula , *Ni-Mn-Ga multifunctional compounds*, Mater. Sci. Eng. A, 481, 80-85, 2008.

[18] O. Söderberg , I. Aaltio , Y. L. Ge , X. W. Liu , S. P. Hannula , *Recent Developments of Magnetic SMA*, Advances in Science and Technology, **59**, 1-10, 2009.

[19] V. A. Chernenko, R. L. Anton, M. Kohl, J. M. Barandiaran, M. Ohtsuka, I. Orue, S. Besseghini, *Structural and magnetic characterization of martensitic Ni–Mn–Ga thin films deposited on Mo foil*, Acta Mater., **54**, 5461-5467, 2006.

[20] M. Kohl, A. Agarwal, V. A. Chernenko, M. Ohtsuka, K. Seemann, *Shape memory effect and magnetostriction in polycrystalline Ni-Mn-Ga thin film microactuators*, Mater. Sci. Eng. A, **438**, 940-943, 2006.

[21] A. Backen, S.R. Yeduru, M. Kohl, S. Baunack, A. Diestel, B. Holzapfel, L. Schultz and S. Fähler, Acta Mater. **58**, 3415, 2010.

[22] M. Thomas, O. Heczko, J. Buschbeck, U.K. Rößler, J. McCord, M. Scheerbaum, L. Schultz and S. Fähler, New J. Phys. 10, 023040, 2008.

[23] J.J. Rhyne, S. Foner, E.J. Jr. McNiff, R. Doclo, *Rare earth metal single crystals; I. High-field properties of Dy, Er, Ho, Tb and Gd*, Journal of Applied Physics, **39** (2), 892-893, 1968.

[24] S. Bundell, *Magnetism in condensed matter*, Oxford University Presse, 2001.

[25] D. Jiles, *Introduction to magnetism and magnetic materials 2nd edition*, Boca Raton, CRC Taylor and Francis, 1998.

[26] P. J. Webster, K. R. Ziebeck, S. L. Town, M. S. *Peak, Magnetic order and phase transformation in Ni2MnGa*, Philosophical Magazine B, **49**(3), 295-310, 1984.

[27]   A. Ayuela, J. Enkovaara, K. Ullakko, R. M. Nieminen, *Structural properties of magnetic Heusler alloys*, J. Phys.: Condens. Matter, **11**, 2017-2026, 1999.

[28]   P Lázpita, J M Barandiarán, J Gutiérrez, J Feuchtwanger, V A Chernenko, and M L Richard, Magnetic moment and chemical order in off-stoichiometric Ni–Mn–Ga ferromagnetic shape memory alloys, New Journal of Physics 13, 033039, 2011.

[29]   P. G. de Gennes, *Effects of Double Exchange in Magnetic Crystals*, Physical Review **118** (1), 141-154, 1960.

[30]   V. V. Kokorin, V. A. Chernenko, E. Cesari, J. Pons, and C. Segui, *Pre-martensitic state in NI-Mn-Ga alloys*, J. Phys.: Condens. Matter **8** , 6457, 1996.

[31]   J. Pons, V. A. Chernenko, R. Santamarta, and E. Cesari, *Crystal structure of martensitic phases in Ni-Mn-Ga shape memory alloys*, Acta Materialia, vol. **48**, pp. 3027-3038, Jul 2000.

[31]   Chernenko, V.A., E. Cesari, V.V. Kokorin, I.N. and Vitenko, *The Development of New Ferromagnetic Shape Memory Alloys in Ni-Mn-Ga System*, Scripta Metallurgica et Materialia, Vol.**33**, pp. 1239-1244, 1995.

[32]   V. A. Chernenko, C. Segui, E. Cesari, J. Pons, and V. V. Kokorin, *Sequence of martensitic transformations in Ni-Mn-Ga alloys*, Phys. Rev. **B57**, 2659 1998.

[33]   N. Lanska, O. Söderberg, , A. Sozinov, Y. Ge, K. Ullakko, & V.K Lindroos, *Composition and temperature dependence of the crystal structure of Ni–Mn–Ga alloys*. Journal of Applied Physics, **95**, 8074, 2004.

[34]   Richard, M., Feuchtwanger, J., Schlagel, D., Lograsso, T., Allen, S. & Ohandley, R., *Crystal structure and transformation behavior of Ni–Mn–Ga martensites*. Scripta Materialia, **54**, 1797-1801 2006.

[35]   S. K. Wu, S. T. Yang, *Effect of composition on transformation temperatures of Ni-Mn-Ga shape memory alloys*, Material Letters, **57**, 4291-4296, 2003.

[36]   M. Ohring, *Materials Science of Thin Films, Deposition and Structure*, Academic Press, San Diego, CA, USA, 2002.

[37]   D. E. Sands, *Introduction to Crystallography*, Dover Publications, Inc., New York, NY, USA, 1969.

[38]   G. Gerald Stoney, *The Tension of Metallic Films Deposited by Electrolysis*, Proceedings of the Royal Society of London. Series A, Containing Papers of a Mathematical and Physical Character, 82(553), 172-175, 1909.

[39]   U. Kocks, *Texture and Anisotropy*, 1st Ed. Cambridge University Press, 1998.

[40]   R. J. Young, Vacuum **44**, 353, 1993.

[41]   X. Jin, M. Marioni, D. Bono, S. M. Allen, R. C. O'Handley, T. Y. Hsu, *Empirical mapping of Ni–Mn–Ga properties with composition and valence electron concentration*, Journal of applied physics **91** (10), 8222-8224, 2002.

[42]   A. Sozinov, A. A. Likhachev, and K. Ullakko, *Crystal Structures and Magnetic Anisotropy Properties of Ni-Mn-Ga Martensitic Phases With Giant Magnetic-Field-Induced Strain*, IEEE Transactions on Magnetics, **38**, 5, 2814-2816, 2002.

[43]   A. L. Roytburd, T. S. Kim, Quanmin Su, J. Slutsker, M. Wuttig, *Martensitic transformation in constrained films*, Acta. Mater., 14, 5095-5107, 1998.

[44]   V.A. Chernenko, J. Pons, E. Cesari, K. Ishikawa, *Stress-temperature phase diagram of a ferromagnetic Ni-Mn-Ga shape memory alloy*, Acta Mat., **53**, 5071-5077, 2005.

[45]   C. V. Thompson, *Grain Growth in Thin Films*, Annu. Rev. Mater. Sci., **20**, pp. 245-268, 1990.

[46]   W. W. Mullins, *The Effect of Thermal Grooving on Grain Boundary Motion*, Acta Met. **6**, 414, 1958.

[47]   C. V. Thompson, *Structure Evolution During Processing of Polycrystalline Films*, Annu. Rev. Mater. Sci., **30**, pp. 158-190, 2000.

[48]   C. Hürrich, S. Roth, H. Wendrock, M. Pötschke, D. Y. Cong, B. Rellinghaus, and L. Schultz, *Influence of grain size and training temperature on strain of polycrystalline $Ni_{50}Mn_{29}Ga_{21}$ samples*, J Phys: Conference Series **303,** 2011

[49]   H. Rumpf, H. Craciunecu, H. Modrow, Kh. Olimov, E. Quandt and M. Wuttig: J. *Magnetism and Magnetic Materials*, **302**, 421, 2006.

[50]   V. A. Chernenko, V. L'vov, J. Pons, and E. Cesari, *Superelasticity in high temperature Ni-Mn-Ga alloys*, J. Appl. Phys. **93**, pp. 2394-2399, 2003.

[51]   V. A. Chernenko, J. Pons, E. Cesari, and K. Ishikawa, *Stress-temperature phase diagram of a ferromagnetic Ni-Mn-Ga shape memory* alloy, Acta Mater. **53**, pp. 5071-5077, 2005.

APPENDIX A

Ni-Mn-Ga XRD Reflection Peak Simulations

Below are the simulated reflection peaks of the Ni-Mn-Ga austenite, non-modulated, 14M, and 10M phases. The simulations were calculated in CrystalDiffract using the lattice parameters of [42].
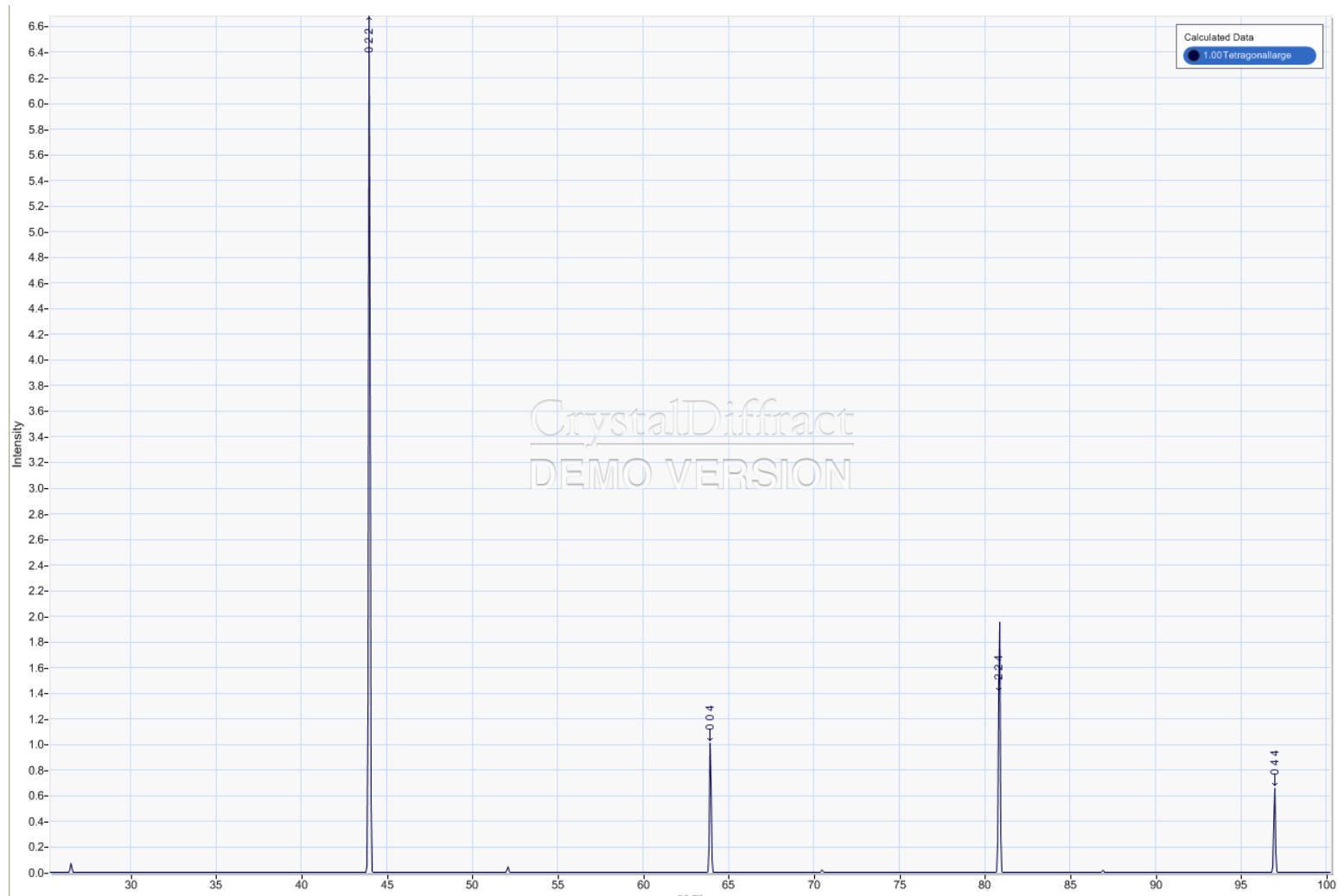
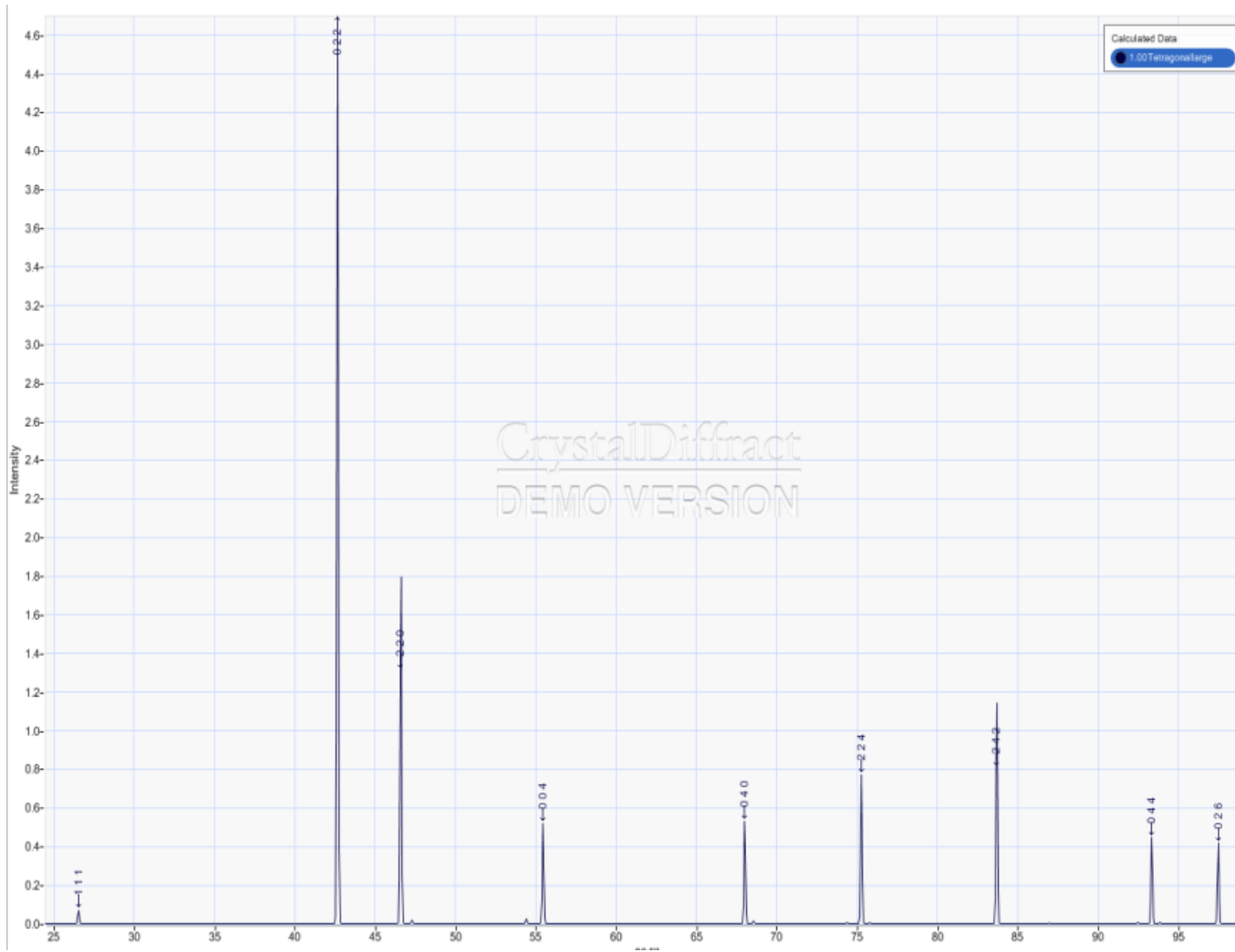**Figure A.1:   Reflection peak simulation of Ni-Mn-Ga austenite structure.**

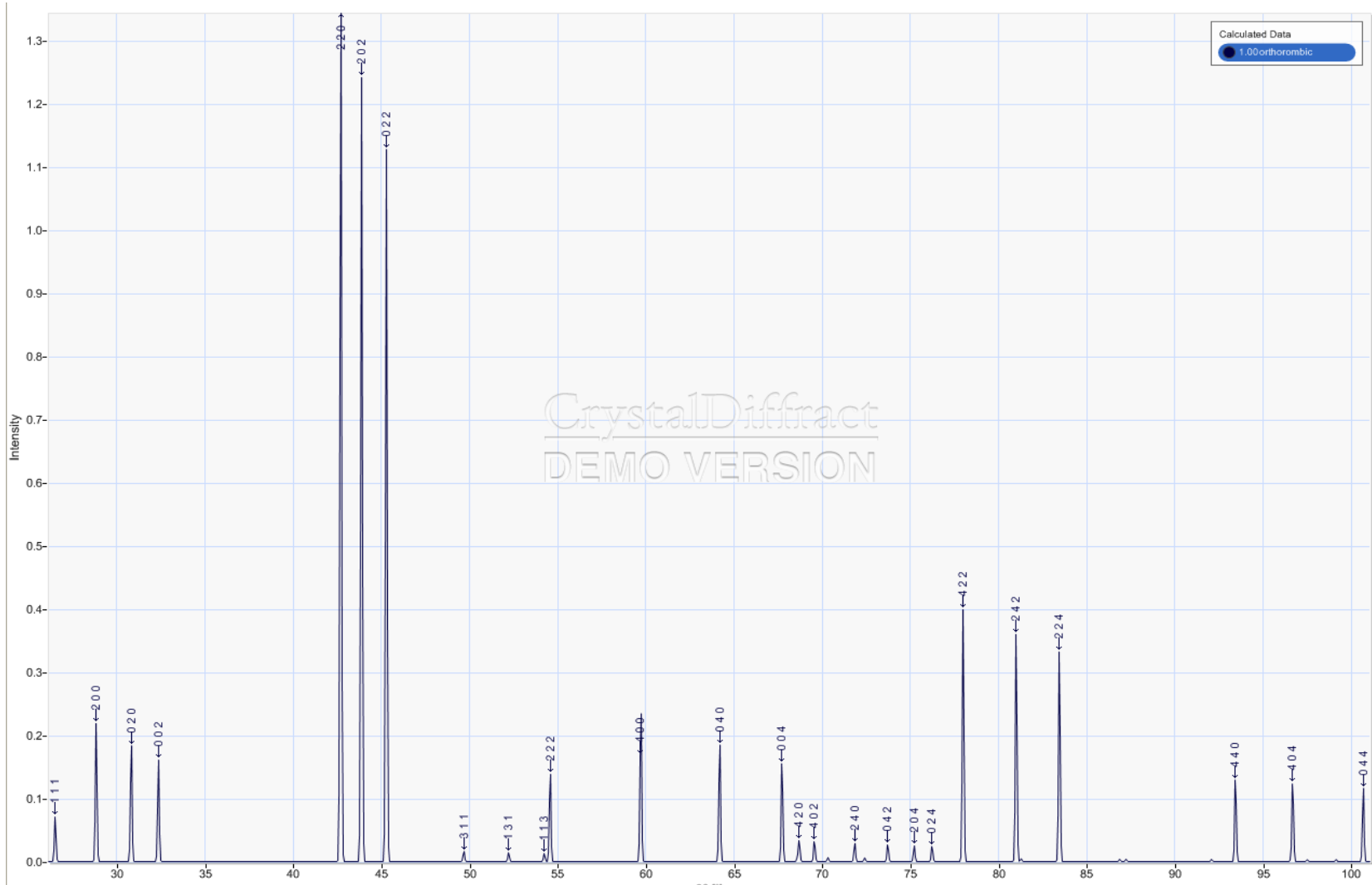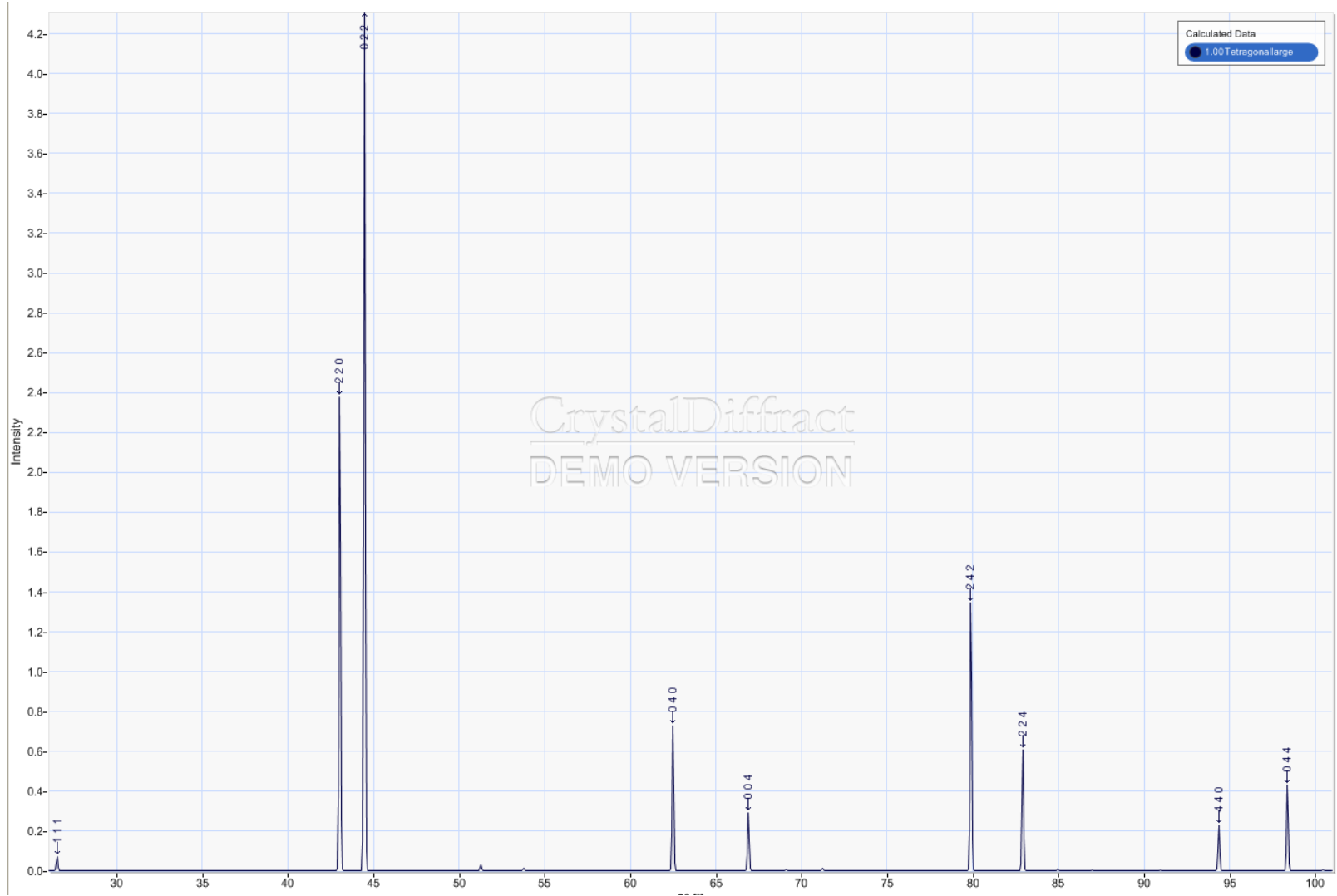**Figure A.2:** Reflection peak simulation of Ni-Mn-Ga NM structure.

Figure A.3:   Reflection peak simulation of Ni-Mn-Ga 14M structure.

Figure A.4: **Reflection peak simulation of Ni-Mn-Ga 10M structure.**